JOURNAL OF GEOPHYSICAL RESEARCH, VOL. 114, A00C20, doi:10.1029/2008JA013528, 2009

First application of a Petschek-type reconnection model with time-varying reconnection rate to THEMIS observations

S. A. Kiehas,[1] V. S. Semenov,[2] M. V. Kubyshkina,[2] V. Angelopoulos,[3] R. Nakamura,[1] K. Keika,[1] V. V. Ivanova,[1] H. K. Biernat,[1,4] W. Baumjohann,[1] S. Mende,[5] W. Magnes,[1] U. Auster,[6] K.-H. Fornaçon,[6] D. Larson,[5] C. W. Carlson,[5] J. Bonnell,[5] and J. McFadden[5]

Received 23 June 2008; revised 21 November 2008; accepted 18 December 2008; published 23 April 2009.

[1] We present a method to determine the location of the reconnection site and the amount of reconnected magnetic flux out of an analytical time-dependent reconnection model and apply this method to disturbances observed on 2 February 2008 at about 0200 and 0815 UT by THEMIS B (P1). During these events, P1 detected two tailward propagating traveling compression regions, associated with typical variations in B_z and B_x. We find the reconnection site to be located at about $-16\ R_E$ for the event at 0200 UT and $-17.5\ R_E$ for the event at 0815 UT. These locations are consistent with simple timing considerations with respect to disturbances detected by the inner THEMIS spacecraft. The amount of reconnected flux in our 2-D model can be found to be in the order of 10^8 nT m for both events. The calculations for the reconnection site's location are done by using two approaches, i.e., by using the B_z and the B_x signals, yielding consistent results. The reconnected flux can be determined using B_z and v_z. Also, these results are in good agreement. A comparison between the disturbances detected by P1 and the modeled variations shows that our model describes disturbances in the magnetic field and the background plasma very well.

Citation: Kiehas, S. A., et al. (2009), First application of a Petschek-type reconnection model with time-varying reconnection rate to THEMIS observations, *J. Geophys. Res.*, *114*, A00C20, doi:10.1029/2008JA013528.

1. Introduction

[2] Within the last decades several attempts were made to describe the energy conversion process of magnetic reconnection in a convincing way. First investigations were based on steady state reconnection [*Sweet*, 1958; *Parker*, 1957; *Petschek*, 1964], which principally can describe the release of a huge amount of energy, but cannot show a temporal evolution of the arising plasma jets, disturbances in the surrounding medium or describe the microscale processes being responsible for reconnection. Latter are the main issue of numerical simulations, which are an important tool to describe reconnection at its heart [e.g., *Birn et al.*, 2001; *Schmitz and Grauer*, 2006]. For effects on the macroscale, i.e., perturbations in the magnetic field and the plasma in the region surrounding the diffusion region, time-dependent reconnection models were established [e.g., *Biernat et al.*, 1987; *Rijnbeek et al.*, 1991; *Semenov et al.*, 2004]. These models provide the opportunity to implement the impulsive character of magnetic reconnection and describe reconnection-associated disturbances in an analytical way. The big advantage of an analytical time-dependent reconnection model is to make allowance to the burst like appearance of reconnection in space plasmas and its possibility to built a quantitative link between the effects of reconnection, which can be observed at a remote site from the initial reconnection site, and the process itself. Thus, several issues of the reconnection process, like the acceleration of plasma, the change in the magnetic field topology, conversion rates, the transport of flux, momentum and energy, or the impulsivity and efficiency of the process can be described quantitatively.

[3] The model in this work is based on the reconnection model, presented by *Biernat et al.* [1987] and *Semenov et al.* [2004], where reconnection is initialized by a time-dependent pulse-like modeled reconnection electric field in a localized part of an infinitely long current sheet, separating two oppositely directed magnetic fields (Figure 1a). During the active phase, i.e., when the reconnection electric field is nonzero, the reconnection associated flow regions are attached to the diffusion region, where the reconnection electric field is active (Figure 1b). During this active or switch-on phase of reconnection, magnetic field

[1]Space Research Institute, Austrian Academy of Sciences, Graz, Austria.
[2]Institute of Physics, State University of St. Petersburg, St. Petersburg, Russia.
[3]IGPP, ESS, University of California, Los Angeles, California, USA.
[4]Institute of Physics, University of Graz, Graz, Austria.
[5]Space Sciences Laboratory, University of California, Berkeley, California, USA.
[6]Institute for Geophysics and Extraterrestrial Physics, Technical University of Braunschweig, Braunschweig, Germany.

0148-0227/09/2008JA013528$09.00

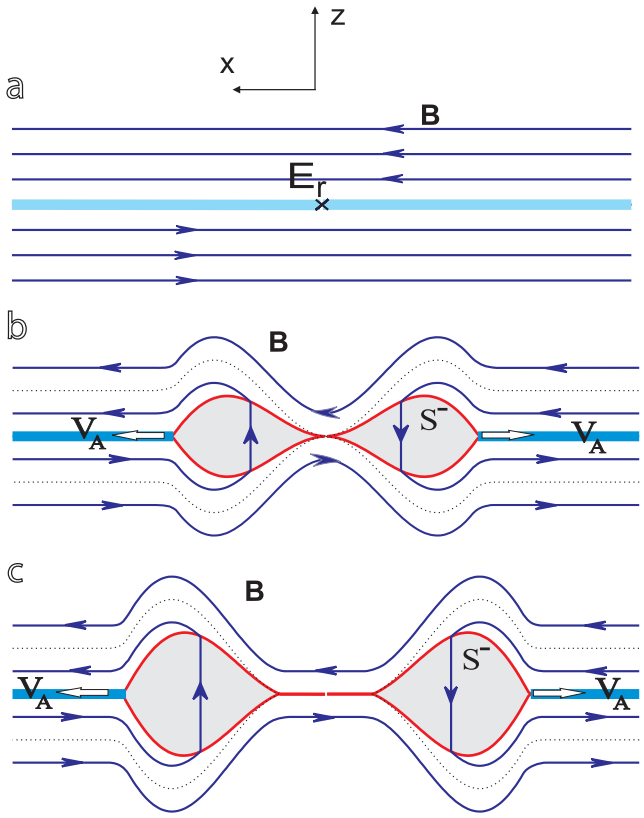

Figure 1. Time-dependent Petschek reconnection for an idealized magnetotail configuration. (a–c) The evolution of the shock structures and the change in magnetic field topology. The coordinate system corresponds to that used for the theoretical model. Reconnection is initiated at the origin. The light blue line denotes a current sheet, separating two antiparallel magnetic fields (blue arrows). Because of the locally and temporally restricted appearance of a reconnection electric field E_r (Figure 1a), plasma gets accelerated and leaves the reconnection site in opposite directions along the current sheet. Because of the temporally restricted activity of E_r, the plasma outflow is confined to closed regions (gray areas, Figure 1b). These regions are bounded by shocks (red) and detach from the initial reconnection site after E_r drops to zero (Figure 1c). Magnetic field lines from both sides of the current sheet are connected via the outflow regions. The dotted lines represent the separatrices [after *Semenov et al.*, 2004].

lines from both sides of the current sheet meet each other at the diffusion region. Since the frozen-in constraint is broken inside this region, field lines are free to reconnect with antiparallel field lines from the opposite side of the current sheet. The inflowing plasma gets accelerated and moves together with the newly reconnected field lines along the current sheet. The field lines are connected via shocks, which enclose the plasma outflow region. If, after some time, the system relapses into the original stable phase of ideal MHD, shown in Figure 1c, the reconnection electric field E_r breaks down (because of its temporally restricted appearance) and the reconnection process switches off and no more reconnected flux is added to the system. At this stage, the switch-off phase, the shocks, bounding the plasma outflow regions and the separatrices bounding the region of reconnected flux, detach from the site where reconnection was initiated. Since the shocks, previously generated during the active phase of reconnection, do not disappear, but detach from the initial diffusion region and propagate with the enclosed outflow region to the edges of the current sheet, the plasma outflow regions cannot be considered as time-independent structures. Thus, the outflow regions display a continuous change in shape and increase in size, because of the accumulation and acceleration of plasma in the outflow regions, even if no more reconnected flux is added. The implementation of a temporally restricted pulse-like reconnection electric field leads to a reconnection onset and switch off, and thus, to a structure of the outflow regions that differs from that in the steady state Petschek model. As the MHD waves propagate away from the diffusion region, the size of the outflow region rapidly outgrows that of the diffusion region. Therefore, this region forms the dominant feature in terms of the conversion and transport of flux, energy and momentum.

[4] In section 2 the framework of this model is shown in more detail. In section 3 we present a method, on the basis of the model from section 2, to determine the location where reconnection was initiated. In order to check if and how the determined location of the reconnection site changes by varying the model input parameter, we evaluate the effects of different reconnection electric fields in the model, shown in section 4. The amount of reconnected flux generated during the reconnection process can be determined out of disturbances in the magnetic field and plasma flow, which is presented in section 5. Thereafter, we apply these methods for the determination of the reconnection site and the amount of reconnected flux to the first two THEMIS events we found during the first tail season in sections 6 and 7. One requirement for the applicability of our method is the detection of typical reconnection-associated disturbances in the surrounding medium. Therefore, we have to confine our investigations to events, during which at least one THEMIS spacecraft was located outside the plasma flow channel. The outermost THEMIS spacecraft P1 and P2 are the most promising probes to observe typical bipolar signatures in the tail magnetic field associated with the propagation of reconnection outflow regions because of their location at about -30 and -20 R_E downtail. Since the inner probes are located at about -10 R_E or closer to the Earth, they are expected to see effects associated with the interaction of an earthward propagating flow with the near-Earth region. The main focus of this work is on the application of our model to P1 data (P2 data was not available during these events). However, we can utilize the advantages of the multispacecraft THEMIS mission by taking observations from the inner spacecraft for timing considerations and check the agreement between onset times at different spacecraft with our determination of the reconnection site. Our results are summarized and discussed in section 8.

2. Analytical Model

[5] We use a 2-D analytical time-dependent reconnection model which can be applied to any plasma and magnetic field environment [*Semenov et al.*, 2004]. For the case of

magnetotail application, we use the simplified and idealized situation of a tangential discontinuity as approximation to the cross-tail current sheet, separating two uniform and identical incompressible plasmas. The initial background magnetic field is represented by two antiparallel magnetic fields on each side of the discontinuity in the form $\mathbf{B}_1 = -\mathbf{B}_2 = (B_0, 0)$, where B_0 is the background magnetic field. Magnetic reconnection requires a breakdown of the ideal (frozen-in) approximation, and thus acts as a dissipative process. Rather than specifying the dissipation mechanism, we model this feature through the introduction of a tangential electric field component $E_r(t)$ inside the small-sized diffusion region, where ideal MHD is broken. Outside the diffusion region, i.e., in the convective region, ideal MHD is valid, and hence, ideal MHD equations can be used to model reconnection-associated disturbances in the surrounding medium:

$$\frac{\partial \mathbf{B}}{\partial t} = \nabla \times (\mathbf{v} \times \mathbf{B}), \tag{1}$$

$$\frac{d\rho}{dt} + \rho(\nabla \cdot \mathbf{v}) = 0, \tag{2}$$

$$\rho \frac{d\mathbf{v}}{dt} = -\frac{1}{4\pi}(\mathbf{B} \times (\nabla \times \mathbf{B})) - \nabla p, \tag{3}$$

$$\nabla \cdot \mathbf{B} = 0, \tag{4}$$

with $\mathbf{B}$, $\mathbf{v}$, ρ, and p as magnetic field, plasma velocity, plasma density and plasma pressure, respectively. All equations appear in CGS units. In the case of ideal MHD, Ohm's Law appears in the reduced form

$$\mathbf{E} + \frac{1}{c}\mathbf{v} \times \mathbf{B} = 0. \tag{5}$$

[6] In order to derive reconnection-associated disturbances in the magnetic field and plasma, we take advantage of the Rankine-Hugoniot jump equations across the shock:

$$[\![m]\!] = 0, \tag{6}$$

$$[\![B_n]\!] = 0, \tag{7}$$

$$\left[\!\left[p + \frac{B^2}{8\pi} + m v_n\right]\!\right] = 0, \tag{8}$$

$$\left[\!\left[m\mathbf{v}_t - B_n \frac{\mathbf{B}_t}{4\pi}\right]\!\right] = 0, \tag{9}$$

$$\left[\!\left[B_n \mathbf{v}_t - m \frac{\mathbf{B}_t}{\rho}\right]\!\right] = 0, \tag{10}$$

where m denotes the mass flow $m = \rho\,(v_n - u_n)$ and u the velocity of the shock normal. Subscripts t and n denote tangential and normal components with respect to the shock, respectively. We divide the system into two regions: the diffusion region, where dissipative processes play an important role and the convective region, where ideal MHD is valid. Our analysis is therefore restricted to the convective region. This region is further subdivided into the outflow region, i.e., the region of outflowing plasma bounded by shocks, and the inflow region, i.e., the convective region around the outflow region. Plasma and magnetic field properties can be expressed through an eight-dimensional MHD state vector [*Semenov et al.*, 2004]:

$$\mathbf{U} = \mathbf{U}(\rho, p, \mathbf{v}, \mathbf{B}),$$
$$\tilde{\mathbf{U}} = \tilde{\mathbf{U}}(\tilde{\rho}, \tilde{p}, \tilde{\mathbf{v}}, \tilde{\mathbf{B}}),$$

where $\mathbf{U}$ and $\tilde{\mathbf{U}}$ denote the state vector in the inflow and outflow region, respectively.

[7] In the case of weak reconnection, the reconnection electric field E_r is much smaller than the Alfvén electric field, $E_A = \frac{1}{c} v_A B_0$, where v_A and B_0 denote the Alfvén velocity and the background magnetic field, respectively. Hence, we introduce the small parameter ϵ:

$$\epsilon \equiv \frac{cE_r}{v_A B_0} \ll 1,$$

which corresponds to a quantitative measure of the reconnection rate, being equivalent to the Mach number M_A used in the analysis performed by *Petschek* [1964]. In contradiction to the original steady state analysis, $\epsilon(\mathbf{r}, t)$ is time-dependent for our investigations. It has to be mentioned that weak reconnection does not imply a weak acceleration process itself. In fact, time-dependent Petschek-type reconnection, as used in this work, acts as fast reconnection, i.e., occurring much more rapidly than the Sweet-Parker reconnection. The restriction to weak reconnection enables us to consider the outflow regions as a thin boundary layer and perform a perturbation analysis of the MHD equations, in which ϵ is used as a small expansion parameter. Thus, the MHD variables can be expanded in the inflow and outflow regions as [see *Kiendl et al.*, 1997]

$$\mathbf{U} = \mathbf{U}^{(0)} + \epsilon\mathbf{U}^{(1)} + \epsilon^2\mathbf{U}^{(2)} + ..$$
$$\tilde{\mathbf{U}} = \tilde{\mathbf{U}}^{(0)} + \epsilon\tilde{\mathbf{U}}^{(1)} + \epsilon^2\tilde{\mathbf{U}}^{(2)} + ..,$$

where $\mathbf{U}^{(0)}$ denotes undisturbed quantities and $\mathbf{U}^{(1)}$ disturbances of the first order. An order of magnitude estimate shows that quantities tangential to the current sheet are of the order of $\sim$1, whereas perpendicular components are of the order of $\sim\epsilon$. Thus, the outflow regions can be treated as thin boundary layer with tangential and normal components corresponding approximately to x and z components, respectively. The MHD variables can then be found by using the following scheme:

$$\mathbf{U}^{(0)} \rightarrow \tilde{\mathbf{U}}^{(0)} \rightarrow \epsilon\mathbf{U}^{(1)} \rightarrow \epsilon\tilde{\mathbf{U}}^{(1)} \rightarrow .. \tag{11}$$

For the purpose of this work, we will not pursue more than the first two steps. First-order effects in the outflow region ($\tilde{\mathbf{U}}^{(1)}$) are discussed by *Alexeev et al.* [2000].

[8] For the inflow region, the zero-order solution is simply given by the background, i.e., the initial parameter values:

$$\mathbf{U}^{(0)} = \mathbf{U}_0.$$

In the following we determine the zero-order components of $\tilde{v}$ and $\tilde{B}$, i.e., the magnetic field and plasma velocity zero-order components in the outflow region [see also *Rijnbeek and Semenov*, 1993; *Semenov et al.*, 2004]. From equations (9) and (10) we obtain the following condition:

$$[\![\mathbf{v}_t]\!] = \pm\frac{[\![\mathbf{B}_t]\!]}{\sqrt{4\pi\rho}},$$

where $\pm$ depends whether v_n and B_n are parallel or antiparallel to each other. Taking into account that tangential and normal components correspond approximately to x and z components, respectively, we furthermore find for the x components of the magnetic field and the plasma flow velocity in the outflow region

$$\tilde{B}_x = 0, \tag{12}$$

$$\tilde{v}_x = \pm\frac{B_0}{\sqrt{4\pi\rho}} \equiv v_A, \tag{13}$$

where positive and negative signs denote a propagation in positive and negative x direction according to the coordinate system in Figure 1. From equation (2) follows

$$\frac{\partial}{\partial z}\tilde{v}_z = 0.$$

The symmetry condition along the x axis requires $\tilde{v}_z(x, 0, t) = 0$, and thus,

$$\tilde{v}_z = 0. \tag{14}$$

For $\tilde{B}_z$ it follows from the induction equation (1) and with equations (13) and (14),

$$\left(\frac{\partial}{\partial t} \pm v_A\frac{\partial}{\partial x}\right)\tilde{B}_z = 0,$$

with the general solution

$$\tilde{B}_z = B_0 g^{\pm}(t \mp x/v_A). \tag{15}$$

The function $g^{\pm}(t \mp x/v_A)$ can be specified by evaluating equation (5) with equations (13) and (15):

$$g^{\pm}(t \mp x/v_A) = \pm\frac{c}{v_A B_0}E_r(t \mp x/v_A).$$

With this, the magnetic field z component in the outflow region appears as

$$\tilde{B}_z = \pm\frac{c}{v_A}E_r(t \mp x/v_A). \tag{16}$$

[9] After this determination of the plasma flow velocity and magnetic field components in the outflow region, we can proceed with the determination of the disturbances in the inflow region, according to scheme (11). For this, we have to determine the shape of the shock, bounding the outflow region. We represent the shape of the outflow region through the function $f(x, t)$. The shock velocity is thus given by $u = f_t$ and the shock normal by $\mathbf{n} = (-f_x, 1)$. With this, and the Alfvén relation, following from equations (9) and (10),

$$\pm(v_n - u_n) = \frac{B_n}{\sqrt{4\pi\rho}},$$

we find for the shape of the outflow region [*Semenov et al.*, 1984; *Biernat et al.*, 1987]

$$f^{\pm}(x,t) = \pm\frac{c}{v_A B_0}xE_r(t \mp x/v_A). \tag{17}$$

For convenience we use normalized quantities in the following. Normalized variables are scaled with respect to the background density ρ_0, background magnetic field B_0, the Alfvén electric field E_A, timescale t_0 and length scale l_0 with $l_0 = v_A\, t_0$. The magnetic field in the outflow regions appears with equation (12) and after normalizing equation (16) as

$$\tilde{\mathbf{B}} = (0, \pm E_r(t \mp x/v_A)). \tag{18}$$

The unknown magnetic field in the inflow region,

$$\mathbf{B} = \left(1 + B_x^{(1)}, B_z^{(1)}\right), \tag{19}$$

can be specified by determining $B_z^{(1)}$. Evaluating the jump condition (7) over the shock, using $\mathbf{n} = (-f_x, 1)$ and the magnetic fields from both sides of the shock from equations (18) and (19) we find

$$-\frac{\partial f}{\partial x} - B_x^{(1)}|_{z=0}\frac{\partial f}{\partial x} + B_z^{(1)}|_{z=0} = \pm E_r(t \mp x/v_A). \tag{20}$$

Neglecting the second term on the left hand side of equation (20) as term of the order of $\mathcal{O}(\epsilon^2)$, we get

$$B_z^{(1)^{\pm}}|_{z=0} = \pm E_r(t \mp x/v_A) + \frac{\partial f}{\partial x}.$$

Inserting $f^{\pm} = \pm xE_r(t \mp x/v_A)$ from normalizing equation (17), the boundary condition for $B_z^{(1)\pm}$ reads

$$B_z^{(1)^{\pm}}|_{z=0} = \pm 2E_r(t \mp x/v_A) - xE_r'(t \mp x/v_A), \tag{21}$$

with $E_r'(t \mp x/v_A)$ as derivative of the reconnection electric field with respect to its argument. In a similar way we find

$$v_z^{(1)^{\pm}}|_{z=0} = -E_r(t \mp x/v_A) \pm xE_r'(t \mp x/v_A). \tag{22}$$

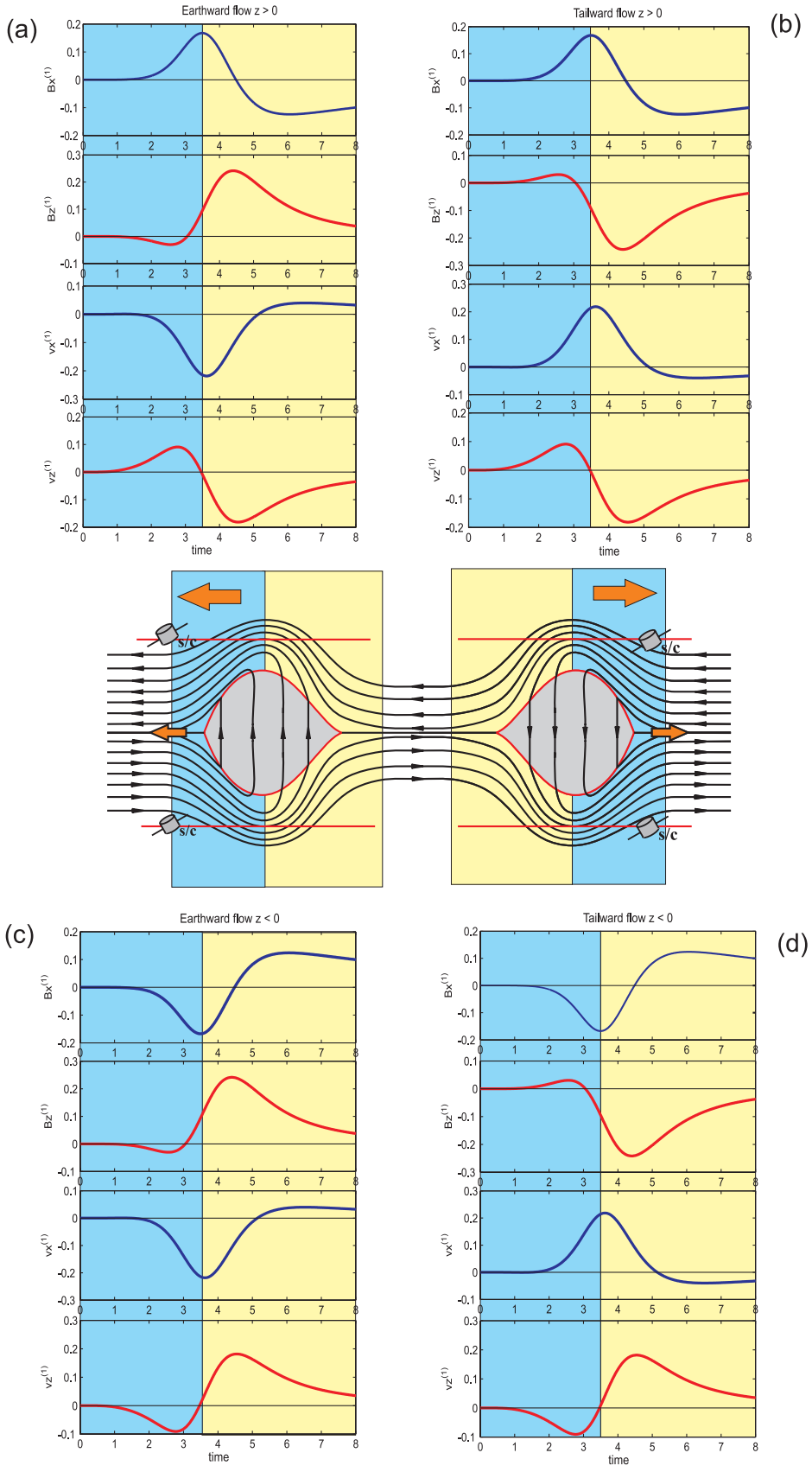
(a)
Earthward flow z > 0
(b)
Tailward flow z > 0
Bx(1)
Bz(1)
vx(1)
vz(1)
time
s/c
(c)
Earthward flow z < 0
(d)
Tailward flow z < 0

Figure 2

Equations (21) and (22) read in dimensional forms,

$$B_z^{(1)^{\pm}}|_{z=0} = \pm 2\frac{c}{v_A} Er\left(t \mp \frac{x}{v_A}\right) - \frac{c}{v_A^2} x E_r'\left(t \mp \frac{x'}{v_A}\right), \quad (23)$$

$$v_z^{(1)\pm}|_{z=0} = -\frac{v_A}{E_A} E_r\left(t \mp \frac{x}{v_A}\right) \pm \frac{x}{E_A} E_r'\left(t \mp \frac{x}{v_A}\right), \quad (24)$$

and correspond to boundary conditions of the disturbances in the magnetic field and plasma velocity z components. With these boundary conditions we can compute the behavior of the magnetic field in the inflow region by solving a Dirichlet problem in the half plane, with the solutions for the x and z components of the magnetic field given by the Poisson integrals [*Vladimirov*, 1984]:

$$B_x^{(1)} = \frac{1}{\pi}\int_{-\infty}^{\infty} \frac{(x-x')B_z^{(1)^{\pm}}|_{z=0}}{(x-x')^2+z^2} dx' \quad (25)$$

and

$$B_z^{(1)} = \frac{z}{\pi}\int_{-\infty}^{\infty} \frac{B_z^{(1)^{\pm}}|_{z=0}}{(x-x')^2+z^2} dx'. \quad (26)$$

In the same way the plasma velocities in x and z can be computed:

$$v_x^{(1)} = \frac{1}{\pi}\int_{-\infty}^{\infty} \frac{(x-x')v_z^{(1)\pm}|_{z=0}}{(x-x')^2+z^2} dx' \quad (27)$$

and

$$v_z^{(1)} = \frac{z}{\pi}\int_{-\infty}^{\infty} \frac{v_z^{(1)\pm}|_{z=0}}{(x-x')^2+z^2} dx'. \quad (28)$$

[10] Equations (25)–(28) describe disturbances in the magnetic field and plasma velocities at any given spacecraft location (x, z) outside the plasma outflow regions. Figure 2 shows these disturbances for different spacecraft positions.

3. Location of the Reconnection Site

[11] The location where reconnection is initiated can be obtained by either solving an inverse problem [*Semenov et al.*, 2005; *Ivanova et al.*, 2007], or choosing a direct way [*Kiehas et al.*, 2008]. We address here to the latter problem.

[12] Because of the growth of the plasma outflow region in the z direction, the disturbances of the magnetic field in the surrounding medium change according to the increase in the volume of the outflow region. With increasing distance to the reconnection site in x, the disturbances exhibit a bigger amplitude because of a larger outflow region (see Figure 3). With increasing distance with respect to z, the amplitudes of the disturbances decrease because of a bigger distance to the outflow region (see Figure 4). The topological correspondence for x and z is sketched in Figure 5. Hence, the disturbances in the magnetic field give information about the distance between the observing spacecraft and the initial reconnection site, if a constant propagation speed of the plasma is assumed. Out of our model, we calculate the ratio between the maximum amplitude in B_z to the entire variation range of the B_z disturbance for different locations (x, z). Additionally, we can use the same calculation with respect to the B_x disturbance in order to get a relation between the ratio for B_x and the distance x and z between a disturbance detecting spacecraft and the initial reconnection site. Thus, the ratio corresponds to

$$r_{max/total}^{B_i} = \frac{\max(B_i)}{\max(B_i) + \mathrm{abs}(\min(B_i))} \quad (29)$$

for disturbances appearing at $x > 0$ (i.e., earthward propagating disturbances), and

$$r_{max/total}^{B_i} = \frac{\mathrm{abs}(\min(B_i))}{\max(B_i) + \mathrm{abs}(\min(B_i))} \quad (30)$$

for disturbances appearing at $x < 0$ (i.e., tailward propagating disturbances), where B_i denotes B_z and B_x, respectively. The resulting 2-D surface functions are shown in Figure 6.

[13] For magnetotail applications, z corresponds to the distance between the spacecraft and the current sheet. By calculating the aforementioned ratios from disturbances detected by spacecraft and determining the distance z of the spacecraft to the current sheet from a T01 model, we can determine the distance x between the spacecraft and the reconnection site. This method is not only very useful to determine the location where reconnection was initiated, but also a necessary basis for calculations on the reconnected magnetic flux, as shown in section 5.

4. Effects of Different Reconnection Electric Fields in the Model

[14] The reconnection electric field is modeled as $E = \sin^2(\pi t)$, active for the time $0 < t \leq 1$, since this function represents the pulsative character of the reconnection process very well. However, also other functions can be used to model the reconnection electric field. In order to test the influence of different pulsative electric fields on the determination of the reconnection site, we compare results obtained by using three different reconnection electric fields: (1) $E_r^1 = \sin^2(\pi t)$, (2) $E_r^2 = \frac{4}{\pi}\sin^2(\frac{\pi}{2}t)$, and (3) $E_r^3 = be^2t^2e^{-bt}$,

Figure 2. Reconnection-associated disturbances detected at different locations with respect to the reconnection site. (a and b) Plots correspond to observations in the upper half plane, i.e., the Northern Hemisphere for magnetotail applications. Disturbances, caused by earthward (Figure 2a) and tailward (Figure 2b) propagating reconnection flow regions in B_x, B_z, v_x, and v_z, are shown. (c and d) Plots show the same situation for the Southern Hemisphere. The color patches in Figures 2a–2d correspond to the patches shown in the central sketch. All calculations are done for the points $x = \pm 3$ and $z = \pm 0.5$. The red horizontal lines in the central sketch symbolize spacecraft trajectories.

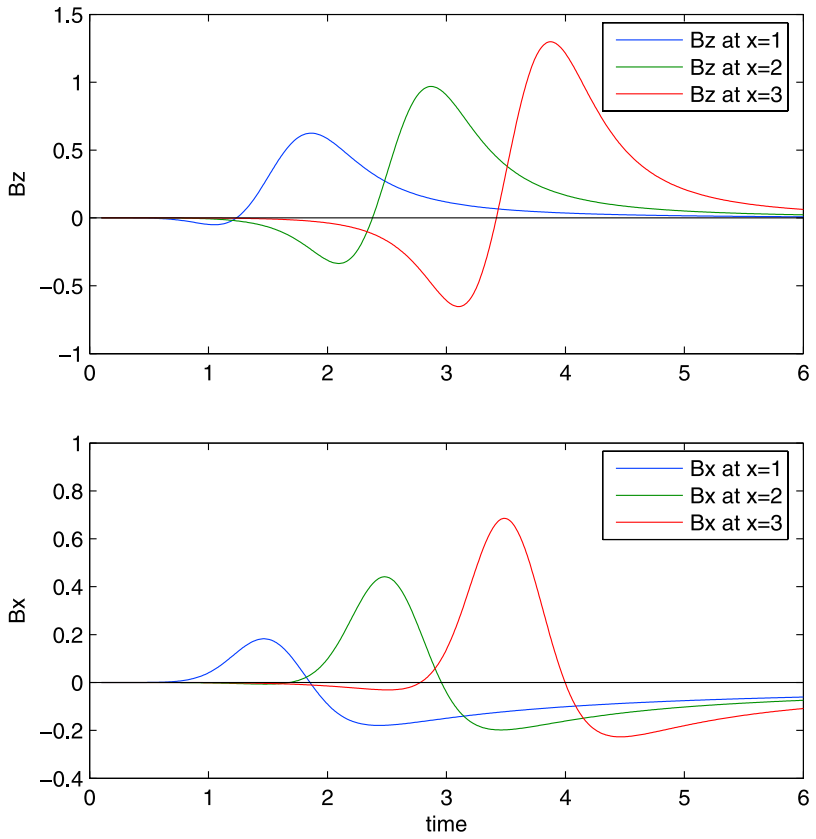

Figure 3. Disturbances in (top) B_z and (bottom) B_x observed at different normalized distances x to the reconnection site (all calculations are done at $z = 0.5$).

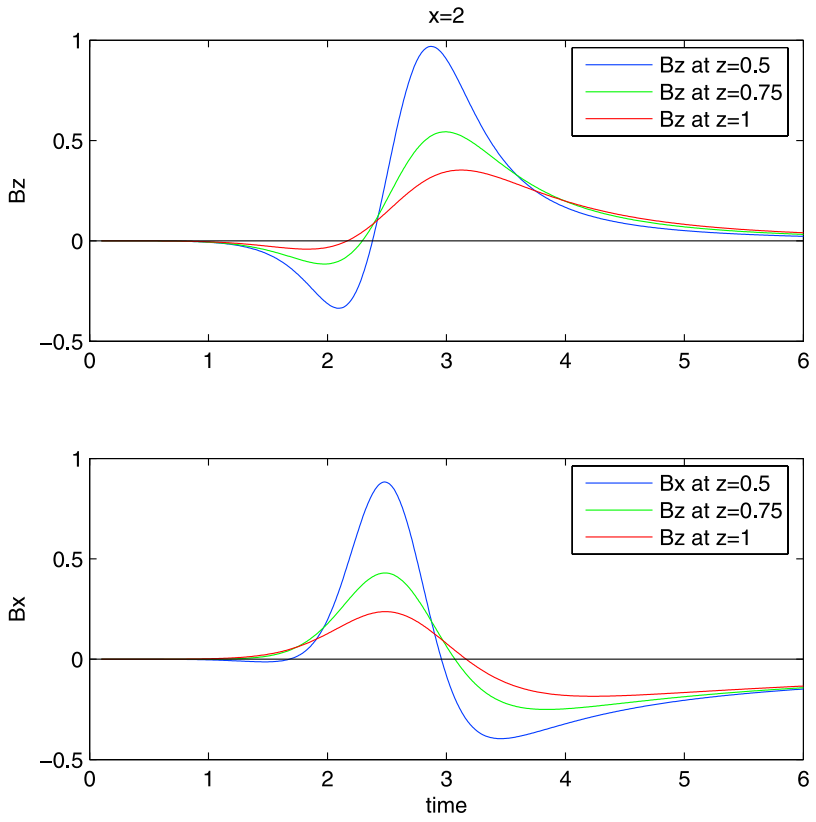

Figure 4. Same as Figure 3 except for fixed $x = 2$ and different distances z.

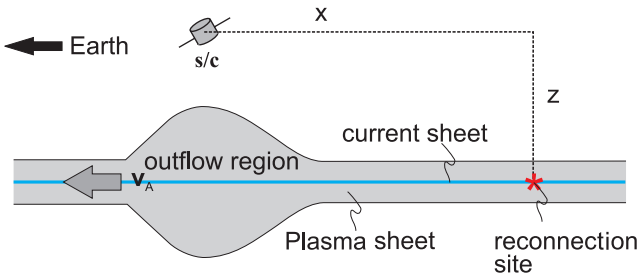

Figure 5. Distances x and z between the reconnection site and a reconnection-associated disturbance-measuring spacecraft for an earthward flow.

with $b = 4$. E_r^1 corresponds to the electric field used for the model, the second one shows the influence of a bigger reconnection rate, slower buildup and longer duration, and the third one exhibits an asymmetric shape with a slightly stronger increase and much slower taillike decrease. All three E_r are shown in Figure 7. As can be seen from Figure 8, the three different electric fields mainly change the magnitude of the magnetic field disturbances, but the general structure remains the same. The second electric field E_r^2 is characterized by a bigger amplitude, and both E_r^2 and E_r^3 exhibit a longer duration than the "standard" one in the model (E_r^1). This leads to a higher reconnection rate; that is, more magnetic flux is reconnected and the size of the outflow region is enhanced. Therefore, the magnetic field in the surrounding medium is more disturbed, as can be seen by larger amplitudes of $B_x^{(1)}$ and $B_z^{(1)}$ in Figure 8.

[15] How is the ratio $r^{B_i}_{max/total}$ from equations (29) and (30) affected by this change? For disturbances generated because of the reconnection electric fields E_r^2, E_r^3, the increase in the amplitude appears for positive and negative variations, but the increase is not strictly linear and thus, $r^{B_i}_{max/total}$ slightly changes, as shown in Figure 9. Figure 9 shows a cut at $z = 1.4$ of the function shown in Figure 6. For a ratio of $r^{B_z}_{max/total} = 0.806$, as obtained for the event discussed in section 6, the function $r^{B_z}_{max/total}(x)$ based on the model with E_r^2 deviates 6.5% from that with E_r^1, and $r^{B_z}_{max/total}(x)$ obtained from E_r^3 deviates 2.75%. Because of different electric fields, also the shock appears to be different. For a longer reconnection electric field the outflow region is bigger at a certain moment in time and $r^{B_z}_{max/total}(x)$ is slightly different at the same observational point (x, z). This is due to a different relative position of (x, z) to the pulse. After rescaling the system, $r^{B_z}_{max/total}(x)$ appears to be the same for different reconnection electric fields.

5. Determination of the Reconnected Flux

[16] We find a clear relation between the integral over B_z and the amount of reconnected flux. The integral over B_z,

$$\int_0^\infty B_z dt = \int_0^\infty dt \frac{z}{\pi} \int_{-\infty}^{\infty} \frac{B_z^{(1)^\pm}|_{z=0}}{(x-x')^2+z^2} dx',$$

can be written by changing the order of integrals, inserting the boundary condition for the case $x' > 0$ from equation (23) and introducing the new variable $\tau = t - x'/v_A$ as

$$\int_0^\infty B_z^+ dt = \frac{z}{\pi} \int_0^\infty \frac{dx'}{(x-x')^2+z^2} \cdot \left(\int_0^\infty 2\frac{c}{v_A} E(\tau) d\tau - \frac{x'}{v_A^2} \int_0^\infty E'(\tau) d\tau \right).$$

With $\int_0^\infty E'(\tau)\, d\tau = 0$ and $c\int_0^\infty E(\tau)\, d\tau = F_0$, where F_0 is the magnetic flux, we find after substituting $(x - x')/z = \xi$, $dx' = -z d\xi$

$$\int_0^\infty B_z^+ dt = -\frac{2F_0}{z v_A \pi} \int_{x/z}^{-\infty} \frac{z d\xi}{\xi^2+1} = -\frac{2F_0}{\pi v_A} \arctan(\xi)|_{x/z}^{-\infty}, \quad (31)$$

$$\int_0^\infty B_z^+ dt = \frac{F_0}{v_A} + \frac{2F_0}{\pi v_A} \arctan(x/z). \quad (32)$$

For disturbances appearing in negative x direction, one finds in the same way

$$\int_0^\infty B_z^- dt = \frac{2F_0}{\pi v_A} \arctan(x/z) - \frac{F_0}{v_A}. \quad (33)$$

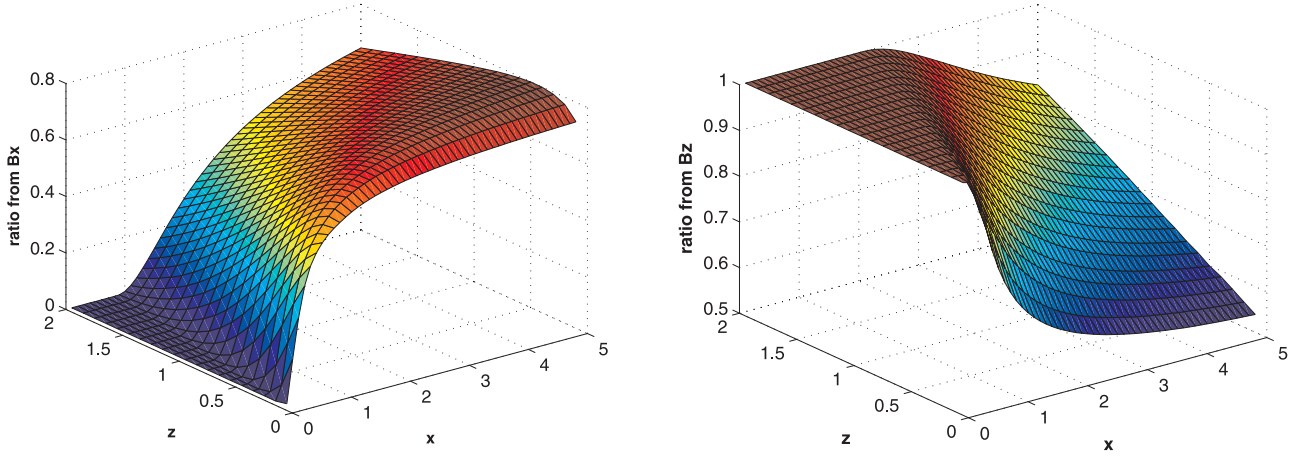

Figure 6. Relation between the ratio $r^{B_i}_{max/total}$ from equation (29) calculated for (left) B_x and (right) B_z and the distances x and z of the observer to the initial reconnection site.

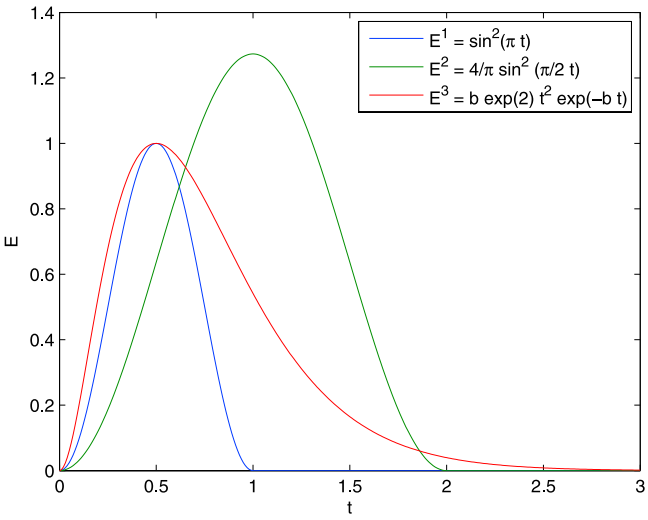

Figure 7. Different pulsative reconnection electric fields. The electric field $E_r{}^1 = \sin^2(\pi t)$ (blue) is used for the model; $E_r{}^2 = \frac{4}{\pi}\sin^2(\frac{\pi}{2}t)$ (green) represents a slower buildup and longer duration; and $E_r{}^3 = be^2t^2\,e^{-bt}$, with $b = 4$ (red), gives a slower taillike decrease, depicting an asymmetric shape.

Equations (32) and (33) yield together

$$F_0 = \frac{\pi v_A}{4\arctan(x/z)}\int_0^\infty B_z dt. \tag{34}$$

Thus, we find the magnetic flux F_0 by integrating B_z over time, knowing the position x and z of the spacecraft with respect to the initial reconnection site and the propagation speed of the outflow regions.

[17] For the integral over v_z,

$$\int_0^\infty v_z dt = \int_0^\infty dt\frac{z}{\pi}\int_{-\infty}^\infty \frac{v_z^{\pm}|_{z=0}}{(x-x')^2+z^2}dx', \tag{35}$$

we find in the same way as for the calculations of $\int_0^\infty B_z\,dt$ by inserting the boundary condition from equation (24) for the case $x' > 0$,

$$\int_0^\infty v_z^+ dt = -\frac{F_0}{2B_0} - \frac{F_0}{\pi B_0}\arctan(x/z), \tag{36}$$

as part of the integral from equation (35) for $x' > 0$.

[18] Inserting the boundary condition (24) we get for the case $x' < 0$

$$\int_0^\infty v_z^- dt = -\frac{F_0}{2B_0} + \frac{F_0}{\pi B_0}\arctan(x/z), \tag{37}$$

as part of the integral for $x' < 0$.

[19] Equations (36) and (37) yield together

$$F_0 = -B_0\int_0^\infty v_z dt. \tag{38}$$

Thus, the integral over v_z yields the amount of reconnected flux, without any dependence on the location, as it is the case for B_z. A physical explanation for this result is sketched in Figure 10. Plasma outside the plasma flow region gets

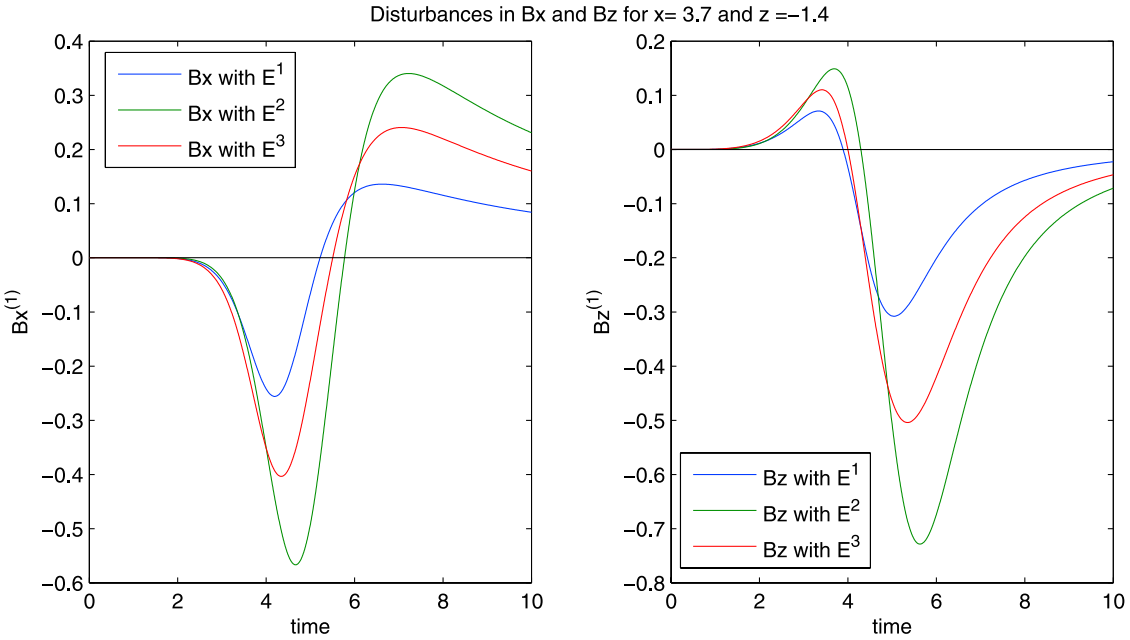

Figure 8. Disturbances in (left) B_x and (right) B_z for three different electric fields (compare Figure 7). Blue: disturbances obtained from the model with $E_r{}^1 = \sin^2(\pi t)$. Green: disturbances obtained from the model with $E_r{}^2 = \frac{4}{\pi}\sin^2(\frac{\pi}{2}t)$. Red: disturbances obtained from the model with $E_r{}^3 = be^2t^2\,e^{-bt}$. Because of a bigger reconnection rate for $E_r{}^2$ and $E_r{}^3$, the disturbances in the magnetic field are stronger, but the ratio between positive and negative variations remains mainly the same. The calculations are made at the point $x = 3.7$, $z = -1.4$.

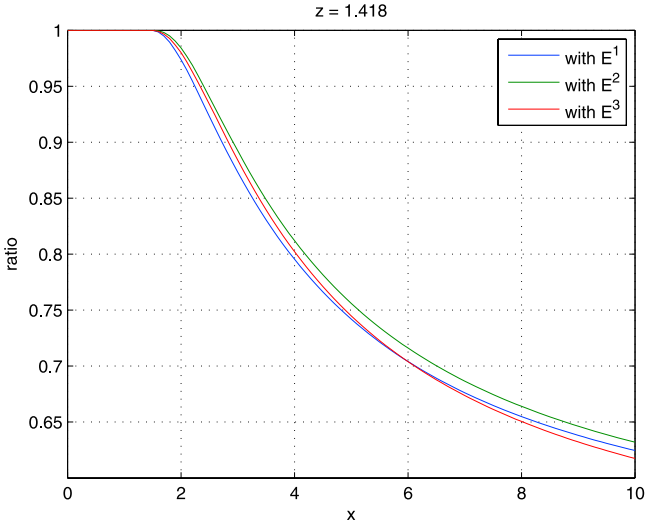

Figure 9. Function $r^{B_z}_{max/total}(x)$ with $z = 1.4$ for B_z resulting from the model with $E^1_r = \sin^2(\pi t)$ (blue), $E^2_r = \frac{4}{\pi}\sin^2(\frac{\pi}{2}t)$ (green), and $E^3_r = be^2t^2e^{-bt}$ (red). For the event discussed in this work, the deviation between $r^{Bz}_{zmax/total}(x)$ obtained with E^1_r and E^2_r is 2.75% and the deviation for $r^{Bz}_{zmax/total}(x)$ obtained with E^1_r and E^3_r is 6.5%. After rescaling, the ratio is the same. Mind the normalized axis scales.

dispersed during the passage of the flow. Thus, the plasma is lifted in front of the shock and sinks down behind it. The temporal integral over the appearing negative v_z corresponds to the amount of reconnected flux. The negative sign is related to the upper half plane, corresponding to the northern lobe for magnetotail applications.

6. Event on 2 February 2008, ~0200 UT

[20] We use observations made by the THEMIS spacecraft [*Angelopoulos*, 2008] for two events on 2 February 2008 in order to determine the location where reconnection was initiated and to estimate the amount of reconnected magnetic flux transported in the course of these reconnection events. Because of the spacecraft locations during the tail season (mid-December until mid-April), we can take advantage of the aligned positions of the five THEMIS

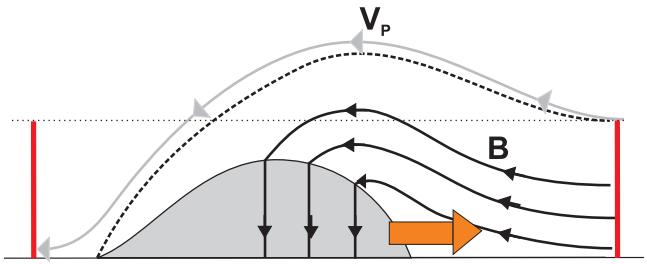

Figure 10. Plasma motion and correlated reconnected flux. Because of the motion of the outflow region, the plasma is lifted in front of the shock and sinks down behind it. The temporal integral over the additional negative velocity component (for observations in the upper half plane, i.e., northern lobe for magnetotail applications) in the z direction (red bar) corresponds to the amount of reconnected flux. The dashed line represents the separatrix.

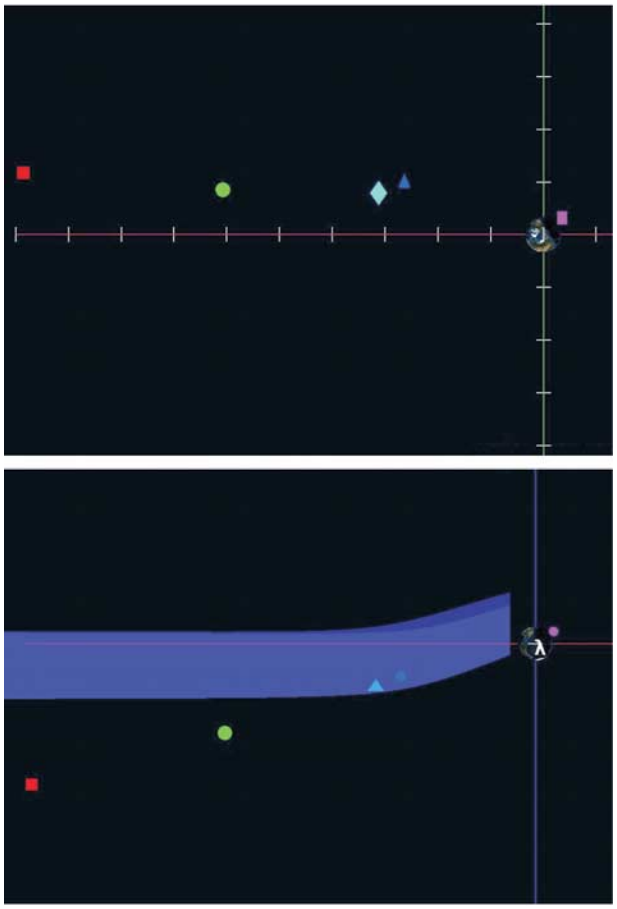

Figure 11. Positions of the THEMIS spacecraft on 2 February 2008 at 0200 UT in (top) the x, y plane and (bottom) the x, z plane: P1 (red), P2 (green), P3 (light blue), P4 (blue), and P5 (magenta; close to perigee). The blue surface denotes the nominal location of the current sheet derived from a Tsyganenko model (obtained via NASA SSCWeb 3-D orbit viewer).

spacecraft. Unfortunately, P2 data experienced a loss in the transmission from a ground station to the operations center, but we can use P1 observations for distant tail signatures and P3, P4, P5 data for investigations of corresponding near-Earth structures. During the first event at about 0200 UT, the operating THEMIS spacecraft were located as shown in Figure 11 and Table 1.

[21] At 0200:05 UT P1 observes a TCR-like signature, [e.g., *Slavin et al.*, 1984, 2005] and P3 and P4 observe dipolarization at 0158:11 UT and 0159:26 UT, respectively (see Figures 12, 13, and 14). Dipolarization observed by P3

Table 1. THEMIS Spacecraft Positions on 2 February 2008, 0200 UT[a]

Spacecraft[b]	x_{GSM} (R_E)	y_{GSM} (R_E)	z_{GSM} (R_E)	NS Distance (R_E)
P1	−29.6	3.5	−8.3	−5.4
P3	−9.4	2.4	−2.6	0.3
P4	−7.9	3.1	−1.9	0.7
P5	1.1	0.9	0.7	

[a]The neutral sheet (NS) distance of the spacecraft is obtained via a Tsyganenko model and taken from the NASA SSCWeb.
[b]P1, THEMIS B; P3, THEMIS D; P4, THEMIS E; P5, THEMIS A.

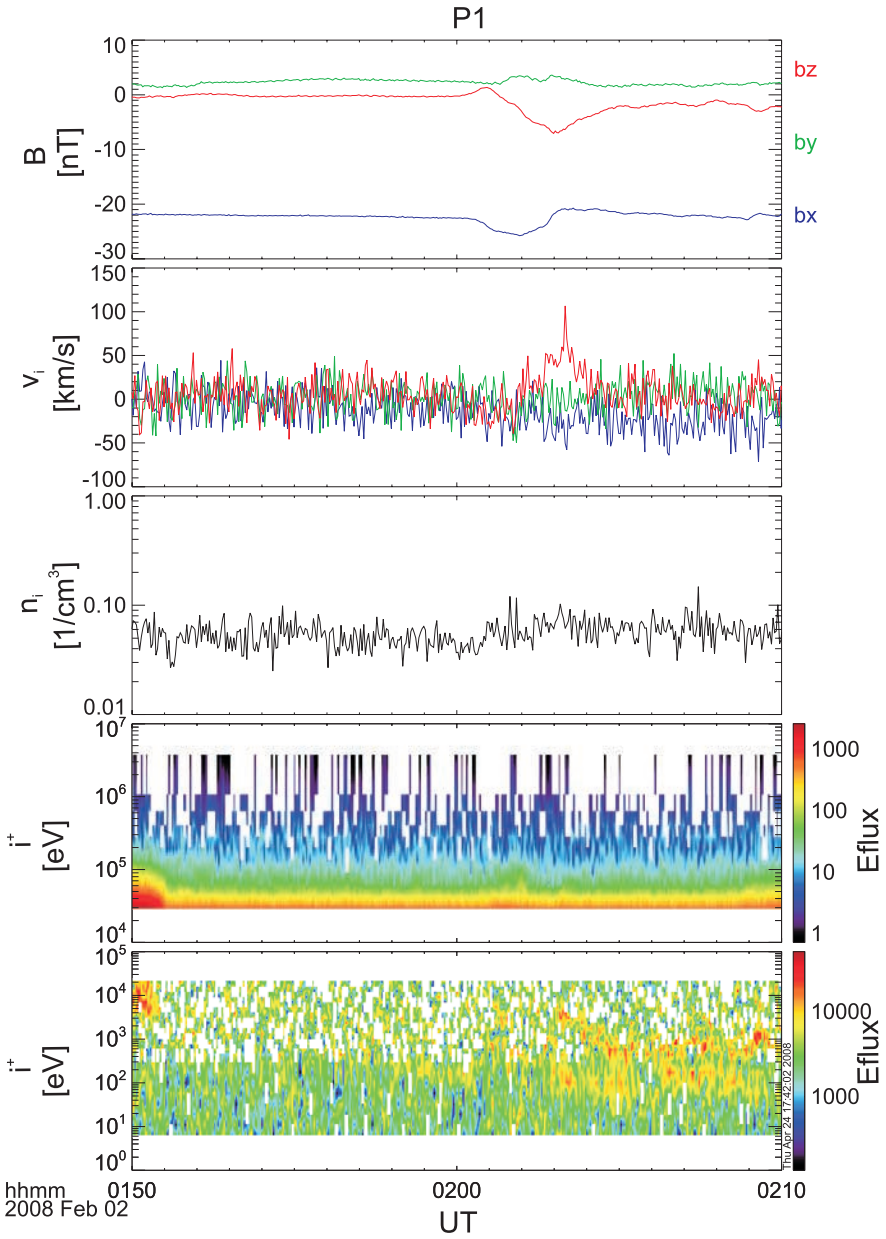

Figure 12. Observations of P1 (THEMIS B) on 2 February 2008 between 0150 and 0210 UT. (first to fifth panels) The plots show the magnetic field B_x (blue), B_y (green), and B_z (red) in GSM coordinates from the FGM instrument [*Auster et al.*, 2008]; the ion velocities v_x (blue), v_y (green), and v_z (red) in GSM coordinates from the ESA instrument [*McFadden et al.*, 2008]; ion density (ESA); and ion energy spectrograms from SST and ESA. As can be seen from the ion velocity and density and the spectrograms, P1 detected no significant plasma flow v_x or enhanced particle flux (indicating that P1 is not inside the plasma outflow region) but observed typical TCR-like magnetic field variations, starting at 0200:05 (compare Figure 15).

can be seen by a decrease in B_x and an increase in B_z, associated with an earthward plasma flow with a peak of ~200 km/s. The initial taillike magnetic field configuration ($B_x \sim 30$ nT, $B_z \sim 10$ nT) changes into a more dipole-like one ($B_x \sim 0$ nT, $B_z \sim 20$ nT).

[22] A similar structure can be seen in the magnetic field data at P4, starting at 0159:26 UT. The time delay between the dipolarization seen on P3 and P4 indicates an earthward propagation of the disturbance. We suggest a relation between the dipolarization seen on P3 and P4 in the near-Earth region with the tailward propagating TCR observed by P1 in the midtail. Within this picture, reconnection appeared somewhere between P3 and P1, leading to a tailward propagating plasma outflow causing the TCR observed by P1 and an earthward moving flow, associated with the disturbances seen on P3 and P4.

6.1. Comparison Between the Model and Observations, ~0200 UT

[23] Figure 15 shows a comparison of the modeled disturbances for a spacecraft positioned at the location of

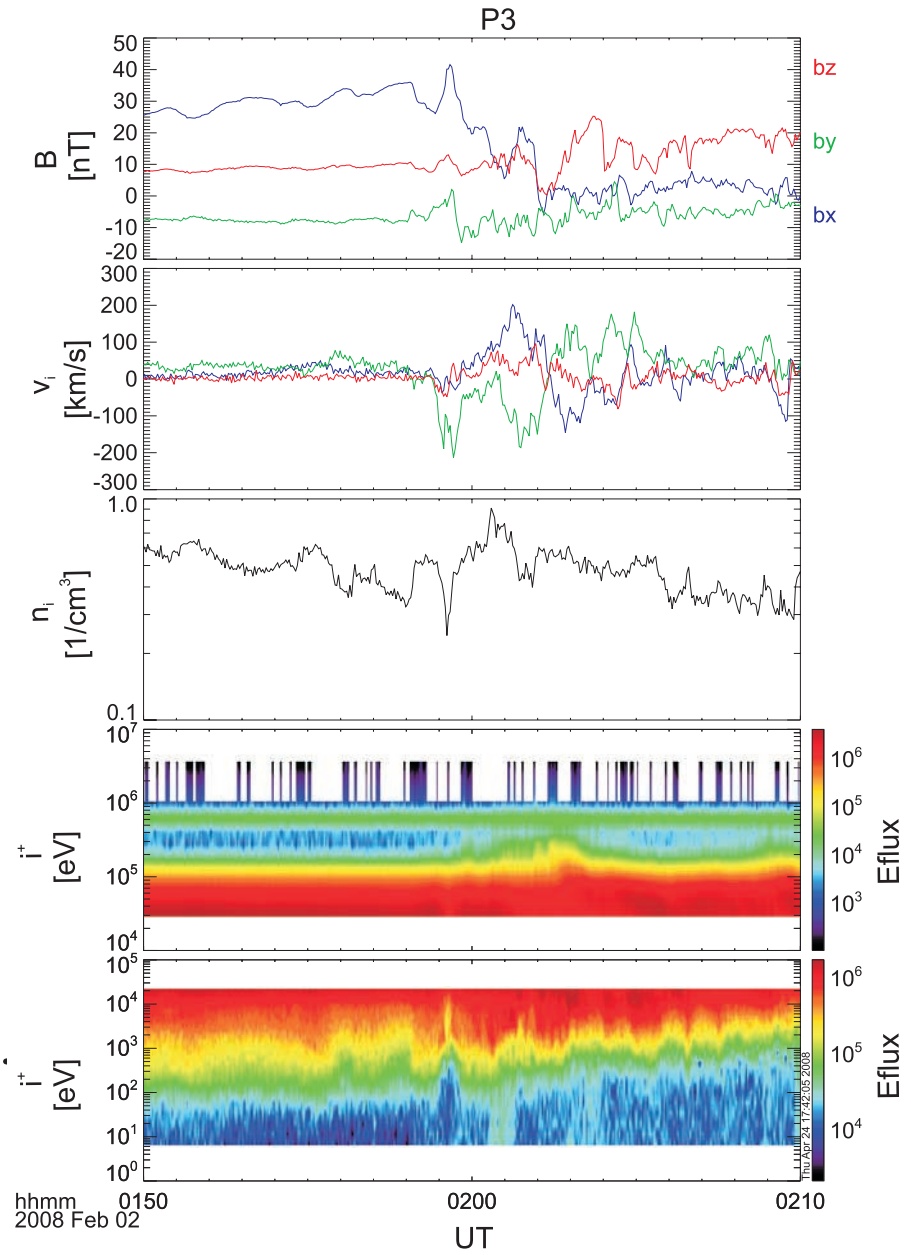

Figure 13. Same as Figure 12 but for observations made by P3. At 0158:11 disturbances in the magnetic field start, leading to a decrease in B_x from about 30−40 to 0 nT and an increase in B_z from about 10 to 20 nT. These magnetic field disturbances are accompanied by earthward flow with a peak of about 200 km/s.

P1 (with respect to the reconnection site) with the observations of P1. We identify the start of the B_z disturbance at P1 to be at 0200:05 UT, when the signal increases. Taking into account a background magnetic field strength of −0.3 nT, the B_z signal reverses at 0201:18 UT from northward to southward, indicating the appearance of a tailward propagating TCR. After a peak of about −6.8 nT with respect to the background B_z, the signal starts to recover. Identifying the end of the main disturbance at 0205:02 UT, the entire duration of the B_z disturbance lasts 4 min and 57 s. In accordance with the theoretical model, B_x first increases at 0200:20 UT and finally gets beneath the background B_x. The maximum in B_x (at 0201:56 UT) appears around the turning in B_z, as predicted by our model. In the plasma velocity data from the ESA instrument, a turning from a first negative v_z to then stronger positive v_z can be seen, with the turning at the time of the maximum in B_x. This is consistent with the picture of lobe plasma moving up and down during the passage of the TCR-associated bulge in the plasma sheet.

6.2. Determination of the X Line Location and the Reconnected Flux

[24] Applying a modified T01 model, the distance of P1 to the current sheet can be found to be 5.35 R_E. Under the assumption of a stretched tail current sheet, the X line location X_r can be found by using equation (30) for the B_z signal at P1 to be at −15 R_E. Applying the same routine to

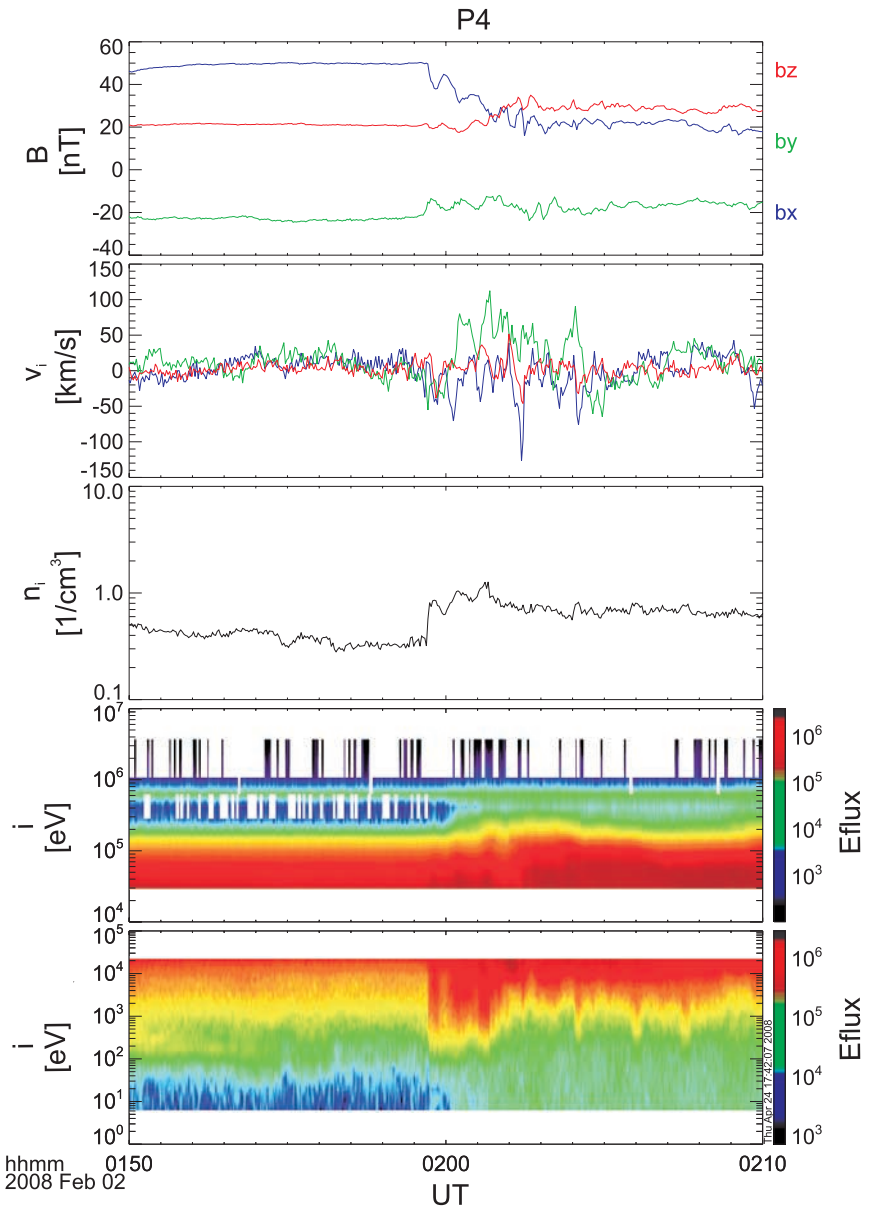

Figure 14. Same as Figure 12 but for observations made by P4. At 0159:26 disturbances in the magnetic field start, leading to a decrease in B_x from about 50 to 20 nT and an increase in B_z from about 20 to 30 nT. From the velocity data, one sees only small short variations in v_x but duskward flow with a peak of about 100 km/s.

B_x, we get $X_r = -16.5\ R_E$. Thus, we conclude an initial reconnection site at about $-16\ R_E$. This location is consistent with simple timing considerations, since P3 with a distance of about 7 R_E to a reconnection site at 16 R_E observes dipolarization 114 s before P1 (about 14 R_E from the reconnection site) detects the TCR. The amount of reconnected flux can be found to be about 1.3×10^8 nT m by using the relation between the integral over B_z from equation (34) and about 0.8×10^8 nT m by using the integral over v_z (equation (38)). Alternatively, the plasma flow velocity can also be obtained by using $\mathbf{E} \times \mathbf{B}$ (see Figure 16). By using v_z from this determination, the amount of reconnected flux can be found to be 1.6×10^8 nT m. The propagation velocity v_A is assumed to be 270 km/s for our calculations, as obtained from timing considerations (see next section).

6.3. Velocity Considerations

[25] We can get a rough idea about the plasma propagation velocity in the tail. If we assume a constant speed between P3 and P1 and a symmetric outflow velocity at the X line, the velocity can be obtained via the simple relation

$$v = \frac{\overline{XP3} - \overline{XP1}}{T_{P3} - T_{P1}}, \tag{39}$$

where $\overline{XP3}$, $\overline{XP1}$, and $T_{P3} - T_{P1}$ denote the distance between the reconnection site and P3, P1, respectively, and the time delay between P3 and P1 (114 s). This yields a

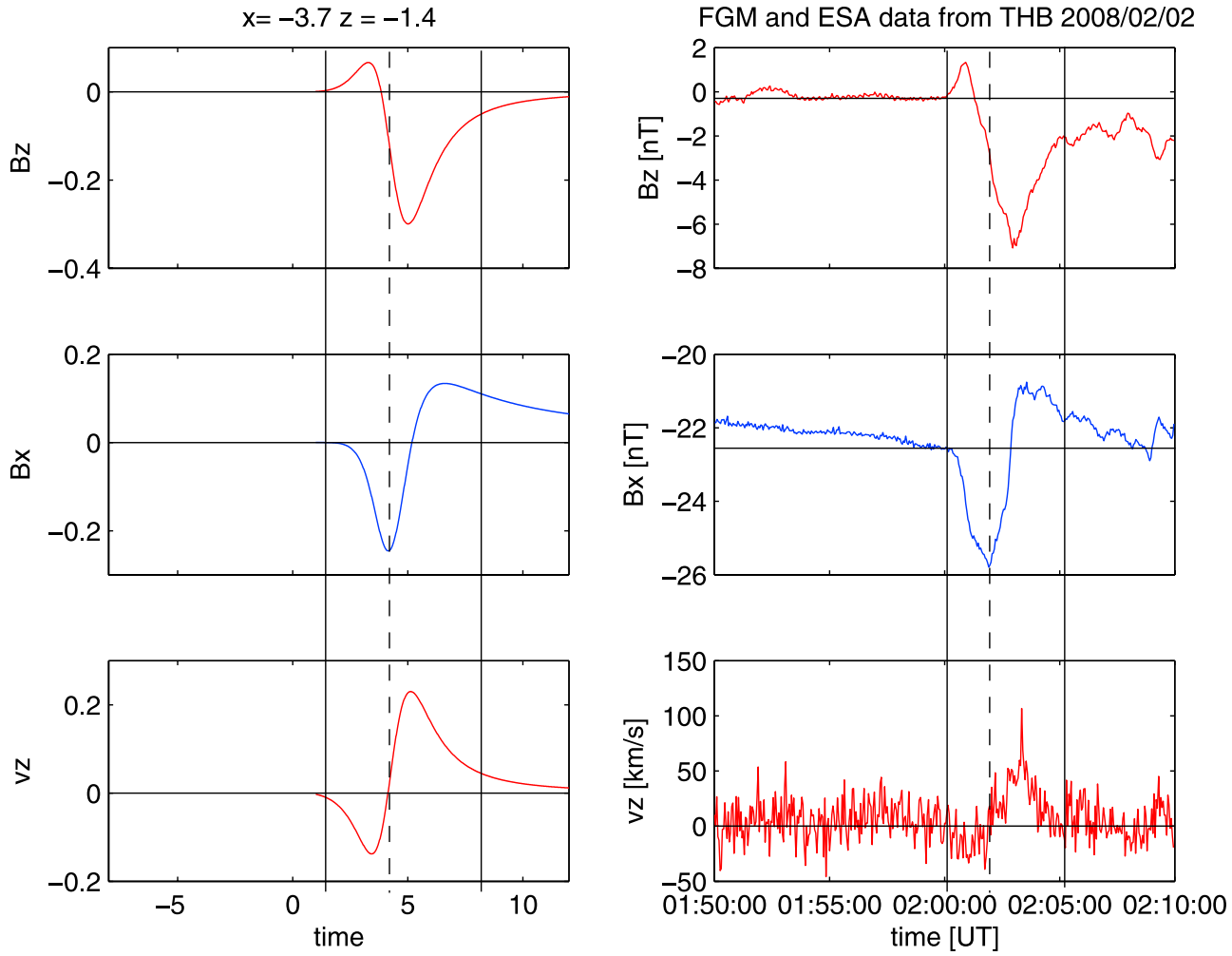

Figure 15. Comparison between our model and the event at ∼0200 observed by P1. (left) The disturbances in B_z, B_x, and v_z, derived from our analytical model. All quantities are plotted in dimensionless units. The calculations are done for a spacecraft located at the same distance to the X line as P1. The x and z values correspond to normalized values. The left vertical solid line represents the beginning of the disturbance in B_z, and the right solid line visualizes the end of the main disturbance. The dashed line represents the maximum in B_x, which corresponds to the turning in v_z and is around the turning in B_z. (right) Observations made by P1 are shown. The vertical lines correspond to those for the model. As can be seen, the observed signatures are reflected by our model very well.

velocity between 330 and 490 km/s for an X line between -15 R_E and -16.5 R_E with an average of about 400 km/s.

[26] On the other hand, the propagation velocity is not constant in the magnetotail because of a magnetic field gradient toward the Earth. Therefore, we suggest a second approach by considering the earthward flow velocity being different to the tailward flow speed. P3 detects earthward plasma flow with a peak of about 200 km/s (compare Figure 13), whereas P4 observes no significant flow in v_x. This suggests flow breaking between about -8 and -10 R_E. Assuming approximately constant plasma propagation speed between the X line and P1, the tailward and earthward flow speeds are

$$v_T = \frac{\overline{XP1}}{T_{P1} - T_X}, \tag{40}$$

$$v_E = \frac{\overline{XP3}}{T_{P3} - T_X}. \tag{41}$$

Expressing T_X from equation (41) and inserting in equation (40) and assuming the detected plasma flow speed on P3 as approximated earthward flow speed, the tailward velocity v_T can be determined via

$$v_T = \frac{\overline{XP1}}{T_{P3} - T_{P1} + \frac{\overline{XP3}}{v_E}}, \tag{42}$$

where v_E denotes the earthward flow velocity, detected at P3. In this case we obtain a tailward flow speed of about 270 km/s. Figure 17 shows calculations of the propagation speed according to equations (39) and (42) for different positions of the reconnection line. As can be seen from Figure 17, the propagation velocity for both approaches is less than 200 km/s for an X line beyond about -18 R_E. Thus, a reconnection site beyond this distance is rather unlikely. Our calculations for the location of the reconnection line

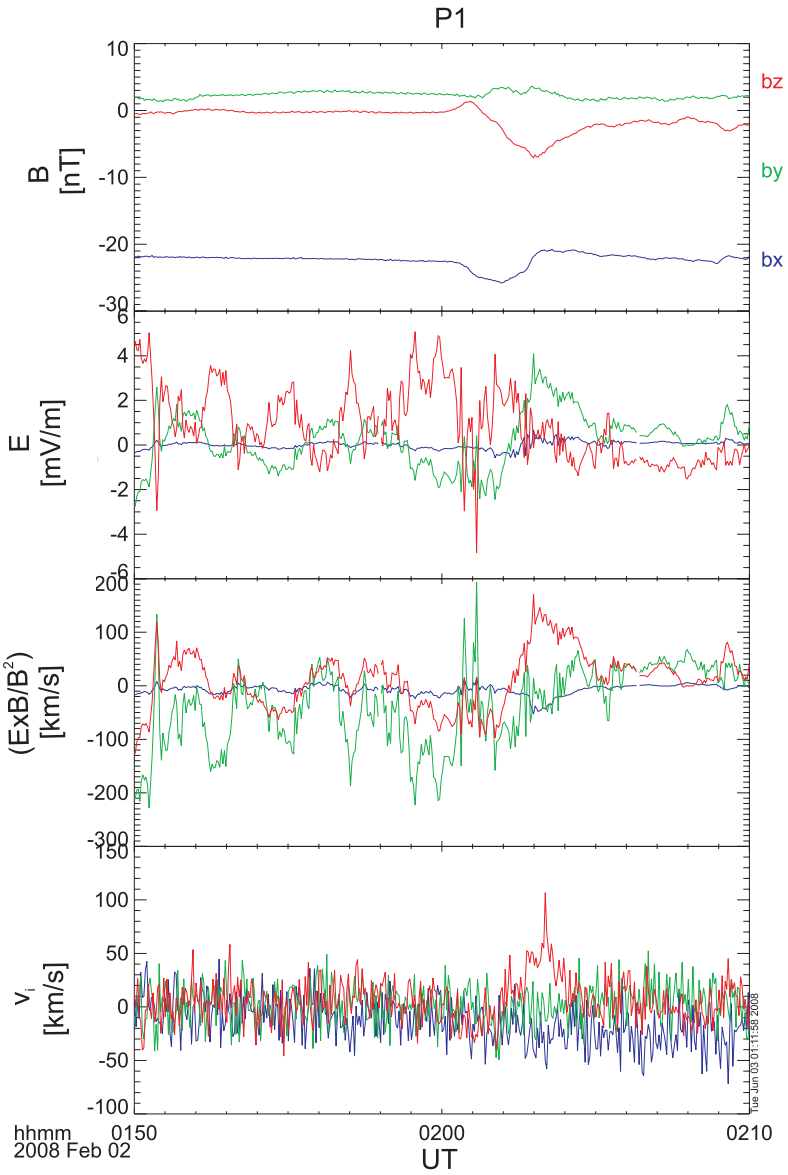

Figure 16. (first to fourth panels) Magnetic field components, electric field (obtained via $\mathbf{E} \cdot \mathbf{B} = 0$ [*Bonnell et al.*, 2008]), plasma velocity obtained via $\mathbf{E} \times \mathbf{B}$, and plasma velocity from the reduced ESA moments data for P1. Blue, green, and red lines denote GSM x, y, and z components.

yield a location of the X line at about 16 R_E and support this qualitative result, obtained via timing considerations.

7. Event on 2 February 2008, ~0815 UT

[27] About 6 h after the previously discussed event, the THEMIS spacecraft observed another event at about 0815 UT. The spacecraft constellation at this time is displayed in Figure 18 and summarized in Table 2.

[28] Figures 19, 20, 21, and 22 display the observations made by P1, P5, P3 and P4. At about 0815 UT, P1 at [−29.7, −0.1, −8.7] R_E GSM detected no enhanced particle flux or significant tailward flow. Some earthward flow can be seen, but since the magnetic structure is tailward propagating (because of the north-to-south reversal in B_z), the flow does not correspond to plasma outflow from the reconnection site, which is assumed to act as source of this structure. Thus, we apply our method to this event. The signatures in the magnetic field are consistent with those of a TCR.

[29] P5 observes disturbances in the magnetic field, starting between 0813:00 and 0813:45 UT, accompanied by earthward flow of about 200 km/s (see Figure 20). Compared to the onset at P1 at 0813:25 UT, both spacecraft observe disturbances almost simultaneously. P3 and P4 observe a gradual increase in B_z, starting at about 0817 UT with no significant flow signatures (see Figures 21 and 22).

7.1. Comparison Between the Model and Observations, ~0815 UT

[30] A comparison between the model and observations by P1 is shown in Figure 23. We identify the onset of the variation in B_z detected by P1 to be at 0813:25 UT with a slight increase in B_z. Taking into account a background B_z of about −1.2 nT, B_z changes from northward to southward

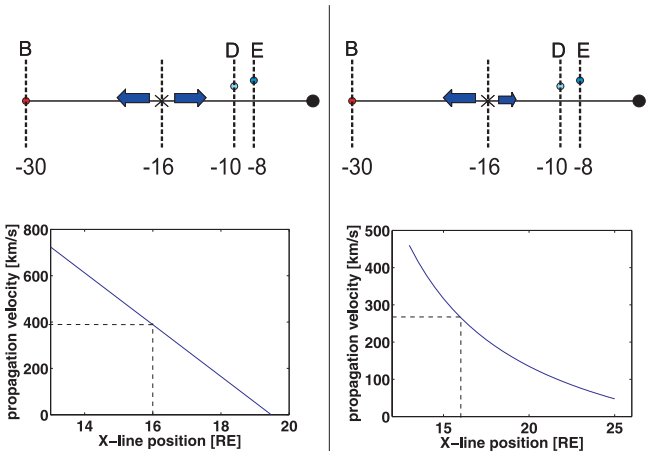

Figure 17. Two different approaches to determine the propagation velocity of the disturbance. (left) Symmetric outflow velocity from the reconnection site is assumed, leading to an average propagation speed of about 400 km/s for a reconnection line at -16 R_E. The bottom left plot shows calculations of the propagation speed according to equation (39) for different locations of the X line. (right) The average earthward propagation speed is assumed to correspond to about 200 km/s, as observed by P3. Thus, the tailward propagation speed can be calculated via equation (42), corresponding to about 270 km/s for an X line at -16 R_E.

at 0814:57 UT. After a negative bay of 5 nT with respect to the background B_z, the signal recovers slowly, as predicted by the analytical model. We see the end of the main disturbance at about 0818:31 UT. The onset in B_x appears at 0814:07 UT, after which B_x reaches a peak of -23.2 nT at 0815:16 UT. After the reversal in B_x and reaching a negative bay, the model predicts a fade-out like it appears in B_z. In fact, the behavior of B_x from P1 after reaching its minimum, is significantly different from the model predictions. B_x increases strongly and reaches a more or less constant value about 3 nT higher than before the event. This can be explained by a sudden plasma sheet thinning or motion, as it can be seen from the energy flux spectrogram in the fifth panel of Figure 19: at about 0818 UT P1 leaves the plasma sheet, accompanied by an increase in B_x. Thus, B_x does not recover slowly to its background value, but increases beyond it.

[31] From the v_z data we see first a plasma flow in the negative z direction, followed by flow in $+z$. This feature corresponds to our model as well, reflecting a motion of lobe plasma because of the appearance of the plasma bulge above the spacecraft.

7.2. Determination of the X Line Location and the Reconnected Flux

[32] The modified T01 model yields a distance between the current sheet and P1 of 5.6 R_E. The ratio r can be found to be 0.54 for B_x and 0.87 for B_z. This gives a distance x between P1 and the X line of 11.9 and 12.4 R_E, respectively. With P1 being located at -29.7 R_E, this yields an X line location at -17.8 R_E and -17.3 R_E, respectively. Thus, we conclude the reconnection site being located at about -17.5 R_E. The amount of reconnected flux, calculated from equation (34) gives a value of 1.1×10^8 nT m. By using the integral over v_z from equation (38), we find 1.2×10^8 nT m. By using v_z obtained via $\mathbf{E} \times \mathbf{B}$, the calculations of the magnetic flux yield 1×10^8 nT m. With an x location of about -17.5 R_E, the reconnection site is located near the middle of P1 and P5, with a distance of $\sim$9 R_E to P5 and $\sim$12 R_E to P1. The onset on P5 can be seen between 0813:00 and 0813:45 UT. Thus, the time delay between P1 and P5 is less than 30 s. This near-simultaneous detection of disturbances can be explained by a bidirectional flow of constant speed from a source located near the middle of P1 and P5. This qualitative assessment is confirmed by the calculation of the reconnection site's location at about 17.5 R_E downtail.

8. Summary and Discussion

[33] Reconnection-associated disturbances in the magnetic field and in the plasma can be modeled by using a time-dependent reconnection model for various locations with respect to the initial reconnection site. A first comparison

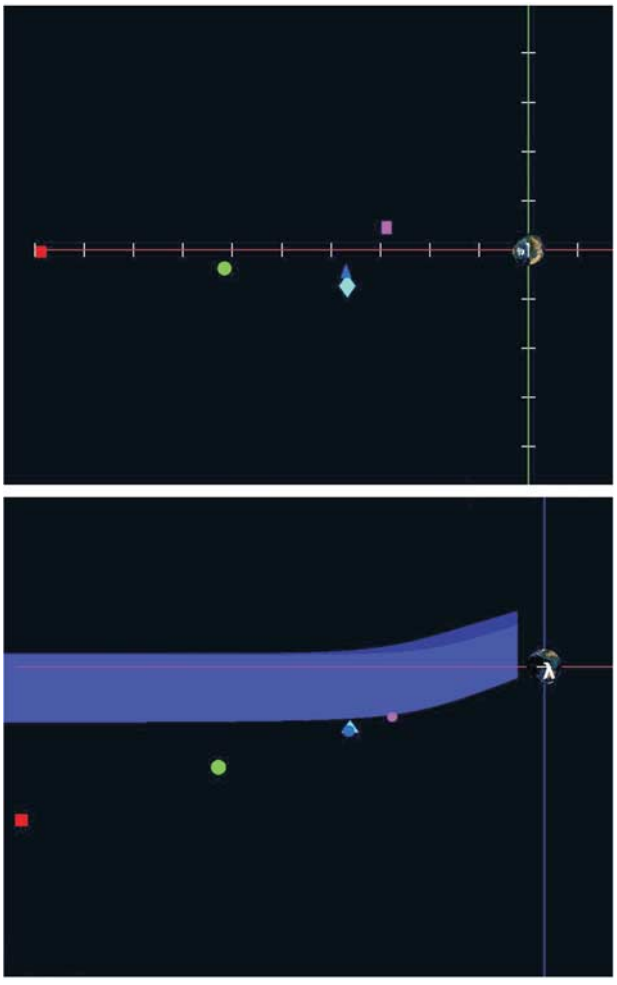

Figure 18. Position of the THEMIS spacecraft on 2 February 2008 at 0815 UT in (top) the x, y plane and (bottom) the x, z plane: P1 (red), P2 (green), P3 (light blue), P4 (blue), and P5 (magenta). The blue surface denotes the nominal location of the current sheet.

Table 2. THEMIS Spacecraft Positions on 2 February 2008, 0815 UT[a]

Spacecraft[b]	x_{GSM} (R_E)	y_{GSM} (R_E)	z_{GSM} (R_E)	NS Distance (R_E)
P1	−29.7	−0.1	−8.7	−5.6
P3	−11	−2.2	−3.5	−0.6
P4	−11.1	−1.3	−3.7	−0.7
P5	−8.7	1.3	−2.9	−0.2

[a]The neutral sheet (NS) distance of the spacecraft is obtained via a Tsyganenko model and taken from the NASA SSCWeb.
[b]P1, THEMIS B; P3, THEMIS D; P4, THEMIS E; P5, THEMIS A.

between these modeled disturbances and observations made by THEMIS spacecraft P1 showed that the modeled variations are in good agreement with the observations in the magnetotail. By using an analytical model, we can get clear relations between these disturbances and the location of the reconnection site and the reconnected flux. For the determination of the reconnection site we apply two methods, by using either disturbances in B_x or in B_z. For the first event, observed by P1 at about 0200 UT, we find the reconnection site by using the B_x signal to be at -16.5 R_E and by using the B_z signal at -15 R_E. For the second event at about 0815 UT, we find -17.8 R_E and -17.3 R_E, respectively. These small differences are beyond the accuracy of this method. Therefore, we conclude an X line location at about -16 R_E for the event at 0200 UT and about -17.5 R_E for the event at 0815 UT. The good agreement between the results obtained by using either B_x or B_z can be seen as verification of the applicability of our method. This can also be seen for the calculations of the reconnected magnetic flux. By using the relation between the flux and B_z, we get for the first event 1.3×10^8 nT m, and by using the direct

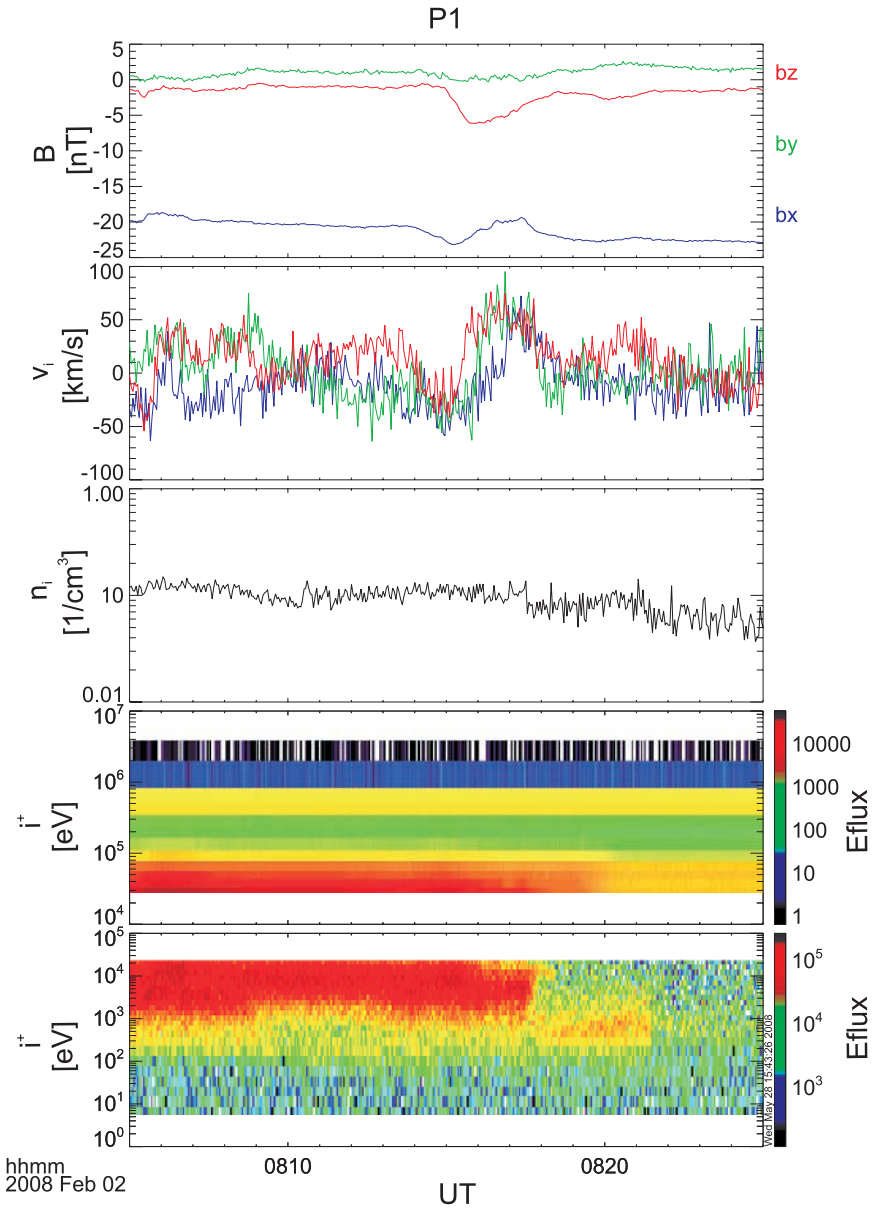

Figure 19. Same as Figure 12 but for the time interval 0805 UT until 0825 UT for P1. According to the ion flow velocities, the ion density, and the ion spectrograms, P1 observed no significant high-speed particle flow but typical TCR structures in the magnetic field, starting at 0813:25 UT.

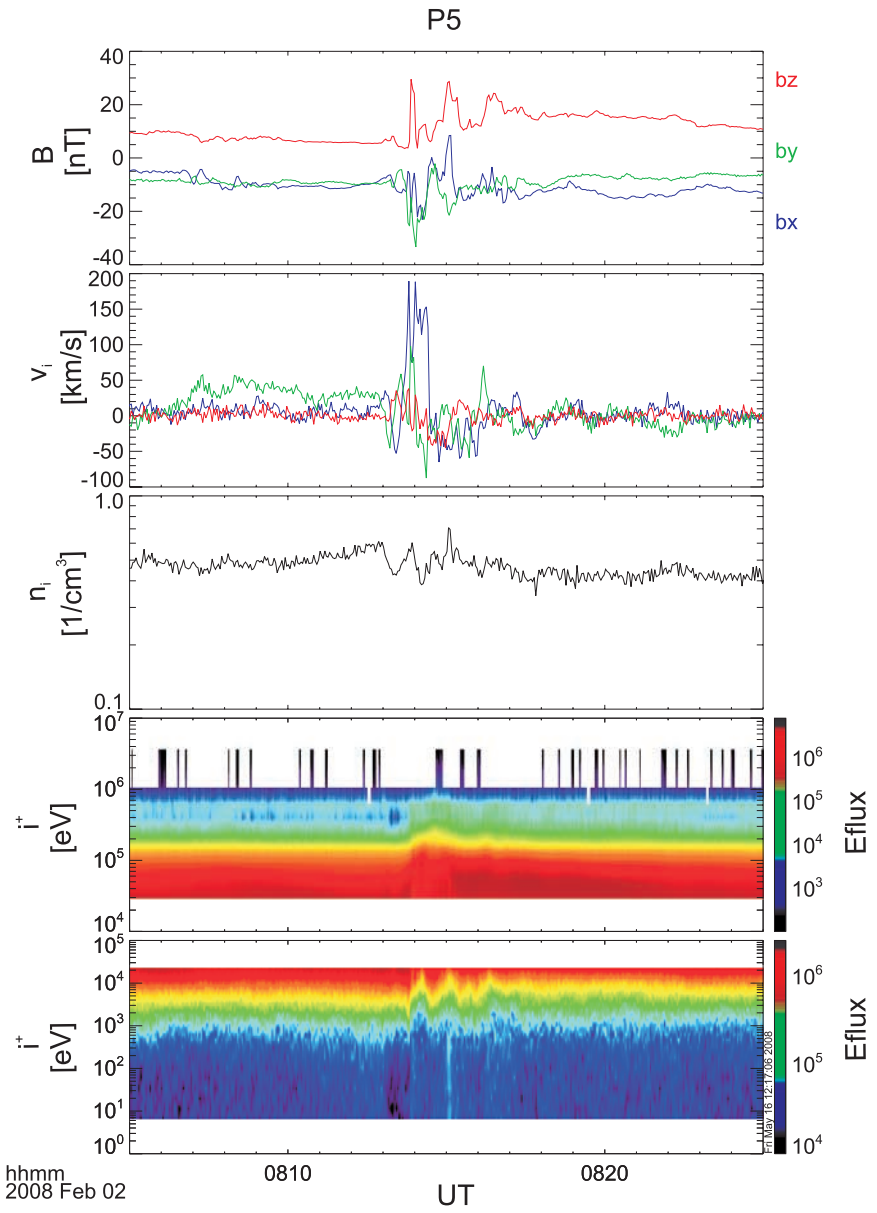

Figure 20. Same as Figure 12 but for the time interval 0805 UT until 0825 UT for P5. Disturbances in the magnetic field start at about 0813 UT, accompanied by earthward flow (peak of about 200 km/s) and enhanced particle flux.

relation with v_z, 0.8×10^8 nT m by using reduced moments data from the ESA instrument and 1.6×10^8 nT m by taking the velocity from $\mathbf{E} \times \mathbf{B}$. For the second event, we find 1.1×10^8 nT m, 1.2×10^8 nT m, and 1×10^8 nT m, respectively. Thus, both methods for obtaining the reconnected flux, i.e., via using magnetic field data and velocity data, work satisfactorily. *Angelopoulos et al.* [1994] determined in a statistical study the BBF-associated transport of magnetic flux by calculating the quantity $E_y = -v_x B_z$. The mean magnetic flux for earthward propagating BBFs was found therein to be 2.6×10^6 Wb/R_E and 4×10^7 Wb/R_E for a single event on 11 April 1985 [*Angelopoulos et al.*, 1996]. These values correspond only to a fraction of the total magnetic flux transport. There are several reasons for this discrepancy, as stated in the mentioned papers. One is due to the determination of the flux transport via obtaining plasma flow v_x and magnetic field B_z, since the result for the magnetic flux transport will depend on the position of the spacecraft with respect to the flow channel. It is possible that the spacecraft does not observe the entire flow, and thus, only a part of the transported flux can be obtained.

[34] For the method presented in this paper, no observations inside the plasma flow are used, but disturbances caused by the propagation of reconnection outflow regions and transported into the surrounding medium. Thus, we obtain more information about the flux transport.

[35] Because of the loss of P2 data, only a comparison between the disturbances measured by the inner spacecraft P3, P4 and P5 with those observed in the midtail by P1 is possible. For the event at about 0200 UT, P5 was located near perigee, but P3 (P4) was positioned at $-9.4\,R_E$ ($-7.3\,R_E$) in the tail, close to midnight.

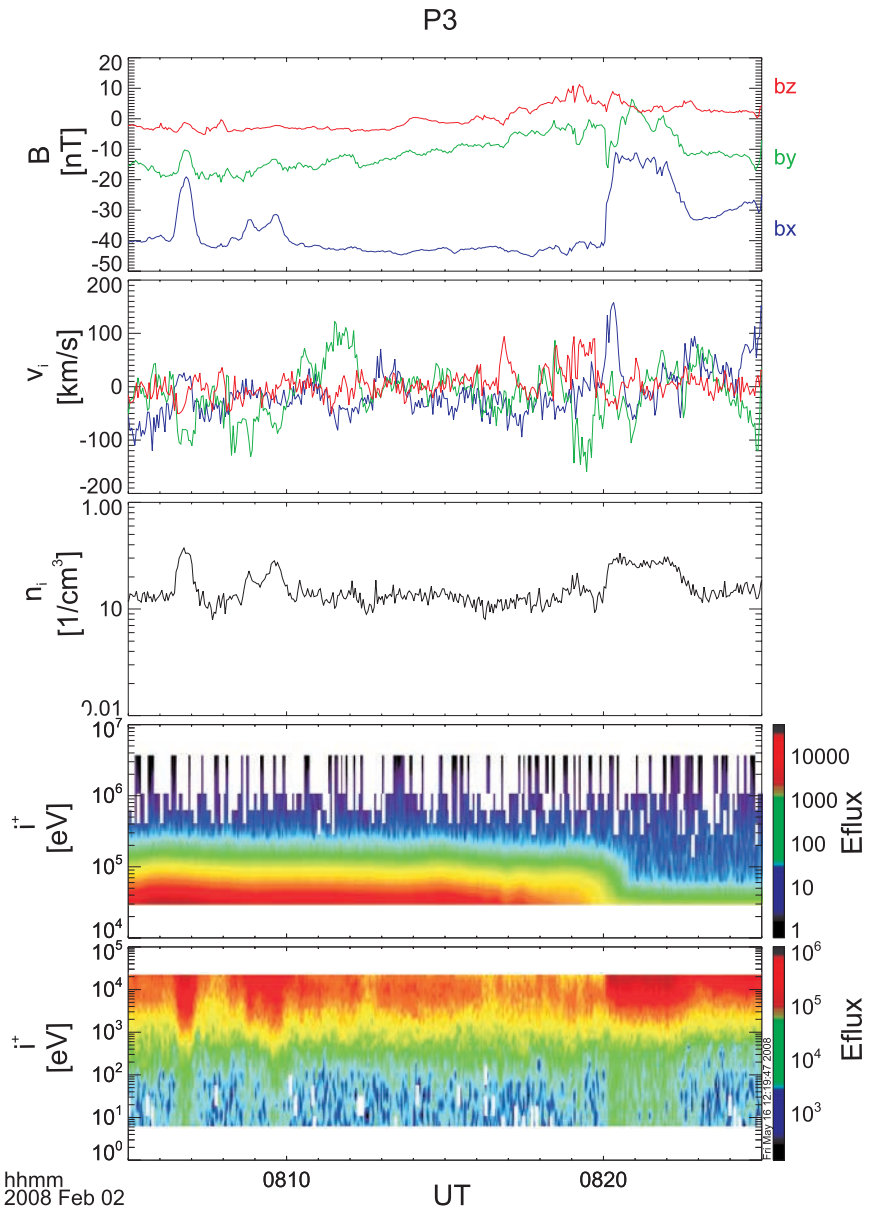

Figure 21. Same as Figure 12 but for the time interval 0805 UT until 0825 UT for P3. At about 0817 a gradual increase in B_z from around 0 to about 10 nT can be seen.

[36] Knowing the position of the reconnection site and the onset time at different spacecraft, an average propagation velocity of the disturbance can be derived. A quantitative assessment of the velocity is hard, since it requires high accuracy in the determination of the position of the X line and the onset timing. For the first event, disturbances detected by P3 appear 114 seconds before the onset on P1. This indicates an X line location closer to P3 than to P1, which is verified by our calculations: The distance of the reconnection site at about -16 R_E to P3 (P1) is about 7 R_E (14 R_E).

[37] For the second event, the onset of disturbances on P5 and P1 appears to be less than 30 s, indicating a reconnection site relatively central in between these two spacecraft, which is also verified by our calculations: The distance of the reconnection site at about -17.5 R_E to P5 (P1) is about 9 R_E (12 R_E). Because of this quasi-simultaneous onset on P5 and P1, the error for the calculations of the propagation speed is rather large.

[38] P3 and P4 observe disturbances later (at about 0817:00 UT, see Figures 21 and 22) than P5, even though they are located about 2 R_E tailward from P5. This might be due to a duskside located source, since P2 and P3 are positioned on the dawn side, but P5 is in the premidnight sector. Ground-based observations support this suggestion.

[39] Altogether, we could determine the location of the reconnection site being at about -16 R_E (-17.5 R_E) for the event at 0200 UT (0815 UT), which is closer to Earth than the statistical studies of *Nagai et al.* [1998] and *Baumjohann et al.* [1999] suggested. However, these studies used Geotail data obtained during the solar minimum. *Nagai et al.* [2005] compared solar wind parameters prior to reconnection onset in the near tail (-25 $R_E < X_{GSM} <$

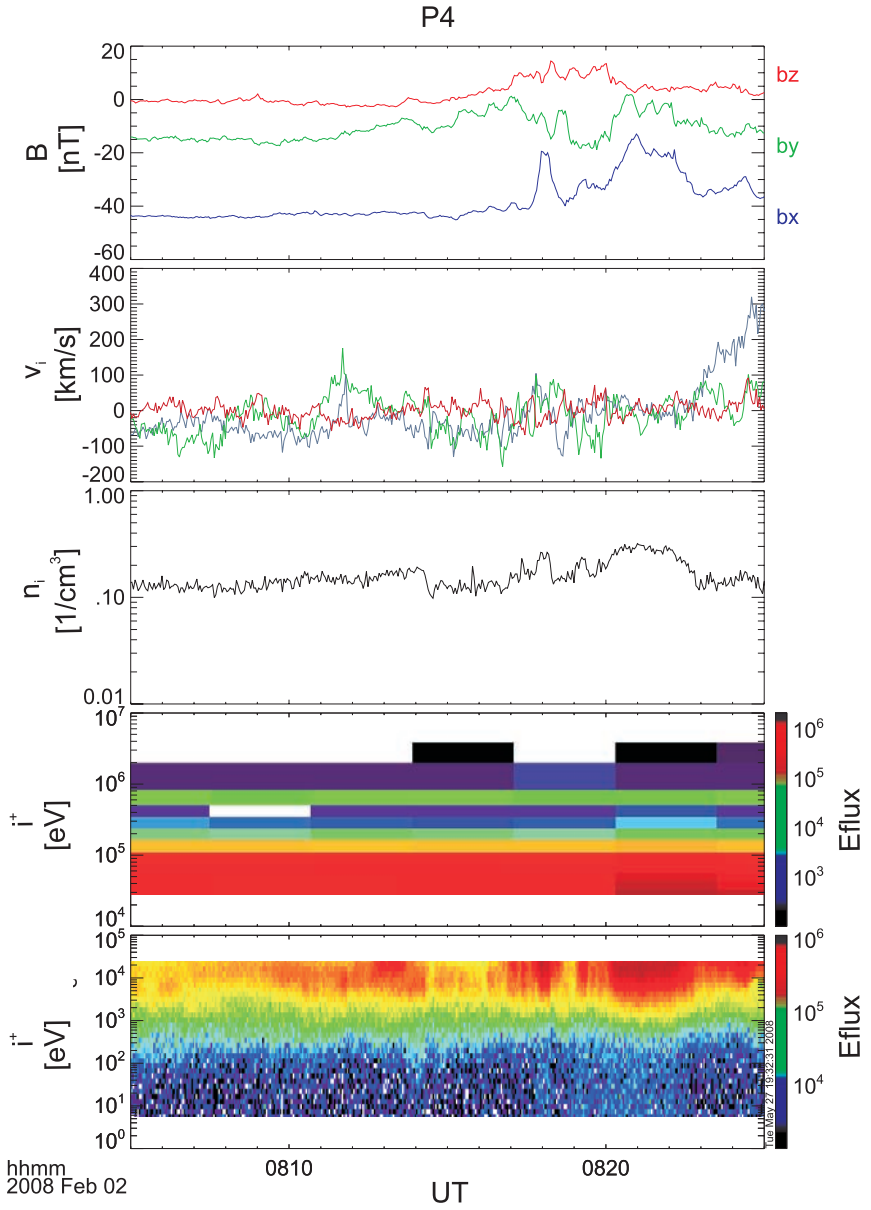

Figure 22. Same as Figure 12 but for the time interval 0805 UT until 0825 UT for P4, with velocity data taken from onboard moments. At about 0817 a gradual increase in B_z from around 0 to about 10 nT can be seen.

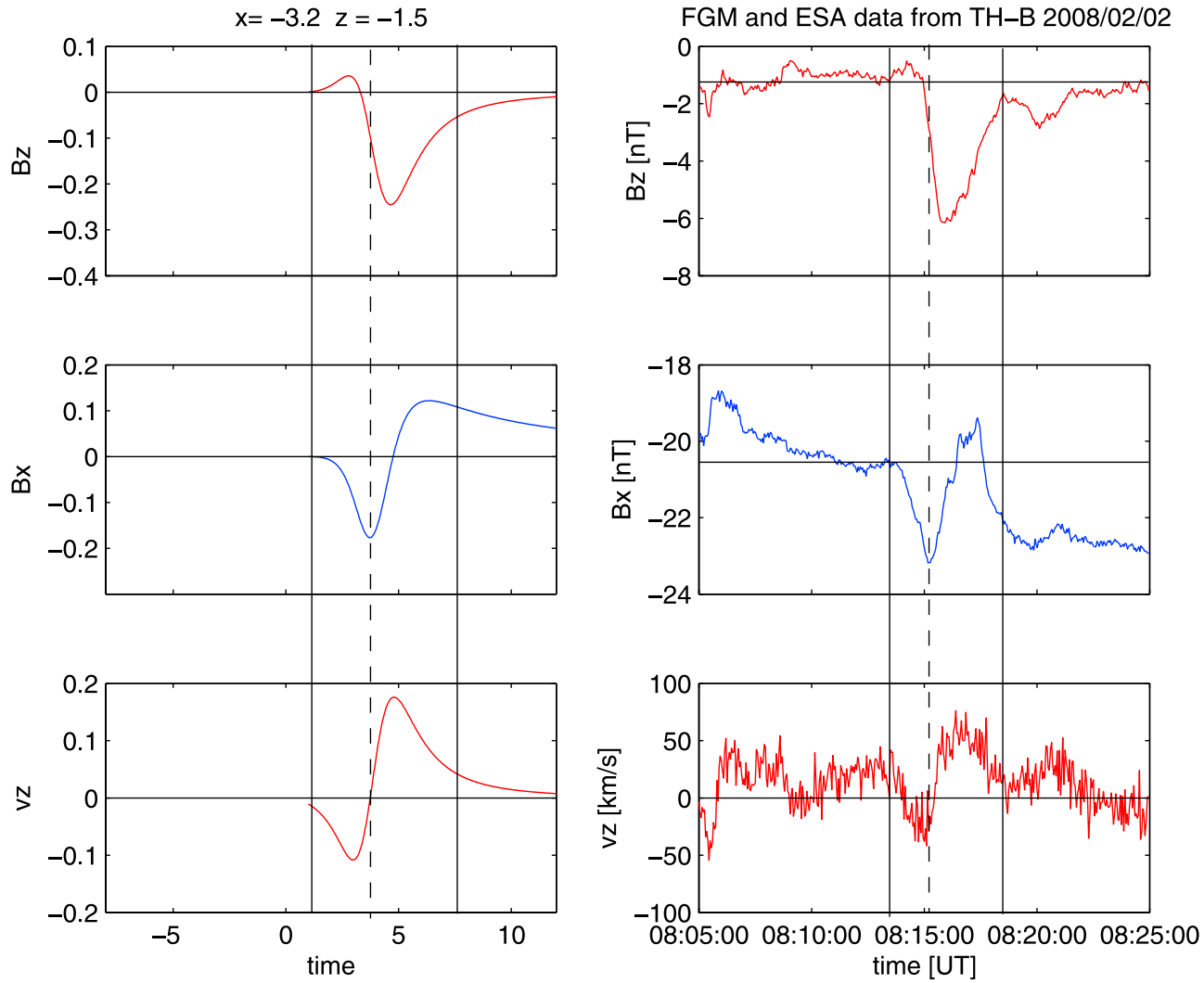

Figure 23. Comparison between our model and the event at ~0815 observed by P1. (left) The disturbances in B_z, B_x, and v_z, derived from our analytical model. All quantities are plotted in dimensionless units. The calculations are done for a spacecraft located at the same distance to the X line as P1. The x and z values correspond to normalized values. The left vertical solid line represents the beginning of the disturbance in B_z, and the right solid line visualizes the end of the main disturbance. The dashed line represents the maximum in B_x, which corresponds to the turning in v_z and is around the turning in B_z. (right) Observations made by P1 are shown. The vertical lines correspond to those for the model. As can be seen, the observed signatures are reflected by our model very well. The differences in B_x after the main disturbance are due to a change in the spacecraft environment (see Figure 19: the spacecraft leaves the plasma sheet after about 0818 UT).

$-15\ R_E$) and midtail ($-31\ R_E < X_{GSM} < -25\ R_E$) by using Geotail data from 1995 to 2003. They concluded that a highly efficient energy input (provided by large southward B_z and high solar wind speed) into the magnetosphere might lead to a reconnection onset rather in the near tail than in the midtail. Prior to the events studied in this work, B_z turned to about -6 nT and the solar wind speed was about 600 km/s. The product $v \times B_z$ of 3600 (km/s) nT corresponds to solar wind conditions, comparable to those during 1999 and 2003 in the Geotail study of *Nagai et al.* [2005]. During this time interval, *Nagai et al.* [2005] found the reconnection onset in the near tail. During less efficient energy input (about 2000 (km/s) nT during 1996 and 1998) the authors found the location of reconnection events in the midtail [see *Nagai et al.*, 2005, Figures 2 and 7].

[40] **Acknowledgments.** This work is supported by the Austrian Fonds zur Förderung der wissenschaftlichen Forschung under project P20341-N16, the Russian Foundation for Basic Research under grant RFBR 07-05-00776a, NASA contract NAS5-02099, and the German Ministry for Economy and Technology and the German Center for Aviation and Space (DLR) under contract 50 OC 0302. Also acknowledged is support by the Verwaltungsstelle für Auslandsbeziehungen, Austrian Academy of Sciences. S.K. acknowledges financial support from the University of Graz in the form of a science support sponsorship (Förderungsstipendium) and thanks Victor Sergeev, Sergey Apatenkov, and Stepan Dubyagin for useful discussions.

[41] Amitava Bhattacharjee thanks Jan Egedal and another reviewer for their assistance in evaluating this paper.

References

Alexeev, I. V., V. S. Semenov, and H. K. Biernat (2000), First-order effects in time-dependent Petschek-type reconnection, *J. Plasma Phys.*, *64*, 547–560.

Angelopoulos, V. (2008), The THEMIS mission, *Space Sci. Rev.*, *141*, 5–34, doi:10.1007/s11214-008-9336-1.

Angelopoulos, V., C. F. Kennel, F. V. Coroniti, R. Pellat, M. G. Kivelson, R. J. Walker, C. T. Russell, W. Baumjohann, W. C. Feldman, and J. T. Gosling (1994), Statistical characteristics of bursty bulk flow events, *J. Geophys. Res.*, *99*, 21,257–21,280.

Angelopoulos, V., et al. (1996), Multipoint analysis of a bursty bulk flow event on April 11, 1985, *J. Geophys. Res.*, *101*, 4967–4989, (Correction, *J. Geophys. Res.*, *102*, 211, 1997.)

Auster, H. U., et al. (2008), The THEMIS Fluxgate Magnetometer, *Space Sci. Rev.*, *141*, 235–264, doi:10.1007/s11214-008-9365-9.

Baumjohann, W., M. Hesse, S. Kokubun, T. Mukai, T. Nagai, and A. A. Petrukovich (1999), Substorm dipolarization and recovery, *J. Geophys. Res.*, *104*, 24,995–25,000.

Biernat, H. K., M. F. Heyn, and V. S. Semenov (1987), Unsteady Petschek reconnection, *J. Geophys. Res.*, *92*, 3392–3396.

Birn, J., et al. (2001), Geospace Environmental Modeling (GEM) magnetic reconnection challenge, *J. Geophys. Res.*, *106*, 3715–3720.

Bonnell, J. W., F. S. Mozer, G. T. Delory, A. J. Hull, R. E. Ergun, C. M. Cully, V. Angelopoulos, and P. R. Harvey (2008), The electric field instrument (EFI) for THEMIS, *Space Sci. Rev.*, *141*, 303–341.

Ivanova, V. V., V. S. Semenov, T. Penz, I. B. Ivanov, V. A. Sergeev, M. F. Heyn, C. J. Farrugia, H. K. Biernat, R. Nakamura, and W. Baumjohann (2007), Reconstruction of the reconnection rate from Cluster measurements: Method improvements, *J. Geophys. Res.*, *112*, A10226, doi:10.1029/2006JA012183.

Kiehas, S. A., V. S. Semenov, I. V. Kubyshkin, M. V. Kubyshkina, T. Penz, H. K. Biernat, and R. Nakamura (2008), Determination of reconnected flux via remote sensing, *Adv. Space Res.*, *41*, 1292–1297, doi:10.1016/j.asr.2007.05.069.

Kiendl, M. T., V. S. Semenov, I. V. Kubyshkin, H. K. Biernat, R. P. Rijnbeek, and B. P. Besser (1997), MHD analysis of Petschek-type reconnection in non-uniform field and flow geometries, *Space Sci. Rev.*, *79*, 709–755.

McFadden, J. P., C. W. Carlson, D. Larson, M. Ludlam, R. Abiad, B. Elliott, P. Turin, M. Marckwordt, and V. Angelopoulos (2008), The THEMIS ESA plasma instrument and in-flight calibration, *Space Sci. Rev.*, *141*, 277–302.

Nagai, T., M. Fujimoto, Y. Saito, Y. S. Machida, S. T. Terasawa, R. Nakamura, T. Yamamoto, T. Mukai, A. Nishida, and S. Kokubun (1998), Structure and dynamics of magnetic reconnection for substorm onsets with Geotail observations, *J. Geophys. Res.*, *103*, 4419–4440.

Nagai, T., M. Fujimoto, R. Nakamura, W. Baumjohann, A. Ieda, I. Shinohara, S. Machida, Y. Saito, and T. Mukai (2005), Solar wind control of the radial distance of the magnetic reconnection site in the magnetotail, *J. Geophys. Res.*, *110*, A09208, doi:10.1029/2005JA011207.

Parker, E. N. (1957), Sweet's mechanism for merging magnetic fields in conducting fluids, *J. Geophys. Res.*, *62*, 509–520.

Petschek, H. E. (1964), Magnetic field annihilation, in *Physics of Solar Flares*, edited by W. N. Hess, *NASA Spec. Publ.*, *50*, pp. 425–439.

Rijnbeek, R. P., and V. S. Semenov (1993), Features of a Petschek-type reconnection model, *Trends Geophys. Res.*, *2*, 247–268.

Rijnbeek, R. P., V. S. Semenov, A. A. Shmalts, H. K. Biernat, M. F. Heyn, and B. P. Besser (1991), Time-dependent reconnection in a current sheet with velocity shear, *Planet. Space Sci.*, *39*, 1377–1395.

Schmitz, H., and R. Grauer (2006), Kinetic Vlasov simulations of collisionless magnetic reconnection, *Phys. Plasmas*, *13*, 092309, doi:10.1063/1.2347101.

Semenov, V. S., I. V. Kubyshkin, M. F. Heyn, and H. K. Biernat (1984), Temporal evolution of the convective plasma flow during a reconnection process, *Adv. Space Res.*, *4*, 471–474.

Semenov, V. S., I. V. Kubyshkin, R. P. Rijnbeek, and H. K. Biernat (2004), Analytical theory of unsteady Petschek-type reconnection, in *Physics of Magnetic Reconnection in High-Temperature Plasmas*, edited by M. Ugai, pp. 35–68, Res. Signpost, Trivandrum, India.

Semenov, V. S., T. Penz, V. V. Ivanova, V. A. Sergeev, H. K. Biernat, R. Nakamura, M. F. Heyn, I. V. Kubyshkin, and I. B. Ivanov (2005), Reconstruction of the reconnection rate from Cluster measurements: First results, *J. Geophys. Res.*, *110*, A11217, doi:10.1029/2005JA011181.

Slavin, J. A., E. J. Smith, B. T. Tsurutani, D. G. Sibeck, H. J. Singer, D. N. Baker, J. T. Gosling, E. W. Hones, and F. L. Scarf (1984), Substorm associated traveling compression regions in the distant tail: ISEE-3 Geotail observations, *Geophys. Res. Lett.*, *11*, 657–660.

Slavin, J. A., E. I. Tanskanen, M. Hesse, C. J. Owen, M. W. Dunlop, S. Imber, E. A. Lucek, A. Balogh, and K.-H. Glassmeier (2005), Cluster observations of traveling compression regions in the near-tail, *J. Geophys. Res.*, *110*, A06207, doi:10.1029/2004JA010878.

Sweet, P. A. (1958), The neutral point theory of solar flares, in *Electromagnetic Phenomena in Cosmical Physics*, edited by E. Lehnert, pp. 123–134, Cambridge Univ. Press, London.

Vladimirov, V. S. (1984), *Equations of Mathematical Physics*, MIR, Moscow.

V. Angelopoulos, IGPP, ESS, University of California, Los Angeles, CA 90095, USA.

U. Auster and K.-H. Fornaçon, Institute for Geophysics and Extraterrestrial Physics, Technical University of Braunschweig, D-38106 Braunschweig, Germany.

W. Baumjohann, H. K. Biernat, V. V. Ivanova, K. Keika, S. A. Kiehas, W. Magnes, and R. Nakamura, Space Research Institute, Austrian Academy of Sciences, Schmiedlstrasse 6, A-8042 Graz, Austria. (stefan.kiehas@oeaw.ac.at)

J. Bonnell, C. W. Carlson, D. Larson, J. McFadden, and S. Mende, Space Sciences Laboratory, University of California, Berkeley, CA 94720, USA.

M. V. Kubyshkina and V. S. Semenov, Institute of Physics, State University of St. Petersburg, St. Petersburg, 198504, Russia.